Harnessing the Oloid Shape in Magnetically Driven Robots to Enable High-Resolution Ultrasound Imaging

Nikita J. Greenidge[1]*, Benjamin Calmé[1], Alexandru C. Moldovan[2], Bartas Abaravicius[3], James W. Martin[1], Nils Marahrens[1], Jon Woolfrey[1], Bruno Scaglioni[1], Damith S. Chathuranga[1], Srinjoy Mitra[3], Sandy Cochran[2], Pietro Valdastri[1]

Magnetic fields enable remote manipulation of objects and are ideal for medical applications, as they pass through human tissue harmlessly. This capability is promising for surgical robots, allowing navigation deeper into the human anatomy and accessing organs beyond the reach of current technologies. However, magnetic manipulation is typically limited to a maximum of two degrees-of-freedom orientation, restricting complex motions, especially those including rolling around the main axis of the magnetic robot. To address this challenge, we introduce a robot design inspired by embodied intelligence and the unique geometry of developable rollers, leveraging the oloid shape. The oloid, with its axial asymmetry and sinusoidal motion, facilitates rolling when precisely controlled by an external magnetic field. We present a versatile closed-loop control model to ensure precise magnetic manipulation of an oloid-shaped robot. This capability was validated in endoluminal applications through the integration of a 28 MHz micro-ultrasound array to perform virtual biopsies – non-invasive real-time histological imaging. Extensive in vitro and in vivo tests using a porcine model showed the robot's ability to execute sweeping motions, identify lesions, and generate detailed 3D scans of gastrointestinal subsurface tissue. This research not only restores a critical movement capability to magnetic medical robots but also enables additional clinical applications deep within the human body.

INTRODUCTION

The application of magnetic manipulation to medical robots, such as robotic catheters (*1*, *2*), flexible endoscopes (*3*–*5*), and capsule endoscopes (NaviCam® (*6*)), has streamlined device design by eliminating the need for complex internal actuation mechanisms (*7*). This approach enables miniaturization and enhances adaptability for navigating intricate anatomical pathways within the body.

Magnetic manipulation involves the use of a controlling magnetic field source to induce a force, $\mathbf{F} \in \mathbb{R}^3(\text{newton})$, and torque, $\boldsymbol{\tau} \in \mathbb{R}^3(\text{newton} \cdot \text{meter})$, on a magnetic object, allowing control over its position and orientation. In medical applications, where the robot is typically considerably smaller than its distance from the controlling field source, the robot behaves as a simple north-south magnetic dipole with a symmetric field around its magnetization axis (denoted by $\mathbf{X}_I$ in Figure 1). As such, magnetic manipulation of objects is typically limited to a maximum of two degrees-of-freedom (DoFs) in orientation and three DoFs in position.

Related works (8–11) have explored the use of magnetic force to produce off-axis rigid body torques to control roll around the object's magnetization axis through various methods detailed in the Results section. However, these techniques, including newer soft magnet methods (12, 13), remain unsuitable in clinical applications. They have only been demonstrated in fluid environments with low force and torque demands, and on micro-scale robots controlled by electromagnetic coil systems. Furthermore, they rely on complex field-generating setups with at least eight magnetic control inputs (*1*, *14*–*16*). A detailed comparison of these approaches, including power consumption and workspace size, is available in Table S1 and the Supplementary Discussion.

In terms of generating the controlling magnetic field, electromagnetic coil systems provide high control precision and adaptability, which are crucial in some applications. However, these systems typically have large physical footprints, limited workspaces, consume substantial power, require cooling, and are expensive to implement (*15*, *17*).

Robotically manipulated single External Permanent Magnet (EPM) systems offer several advantages for slower, larger-scale applications such as flexible endoscopy. These systems require no energy to sustain a static magnetic field, making them energy-efficient and suitable for prolonged use. They can generate strong fields over larger workspaces while being more compact, portable, and cost-effective compared to electromagnetic coil systems (*3*, *18*). The MFE system enables painless (*19*), automated, and remote colonoscopy procedures (*20*) while retaining the same functionalities as standard flexible endoscopes. Although its feasibility has been validated during clinical trials (*19*), it has yet to demonstrate diagnostic capabilities that surpass those of standard flexible endoscopes.

[1]STORM Lab, University of Leeds, Leeds, United Kingdom
[2]University of Glasgow, Glasgow, United Kingdom
[3]University of Edinburgh, Edinburgh, United Kingdom
*Corresponding Author. Email: elnjg@leeds.ac.uk

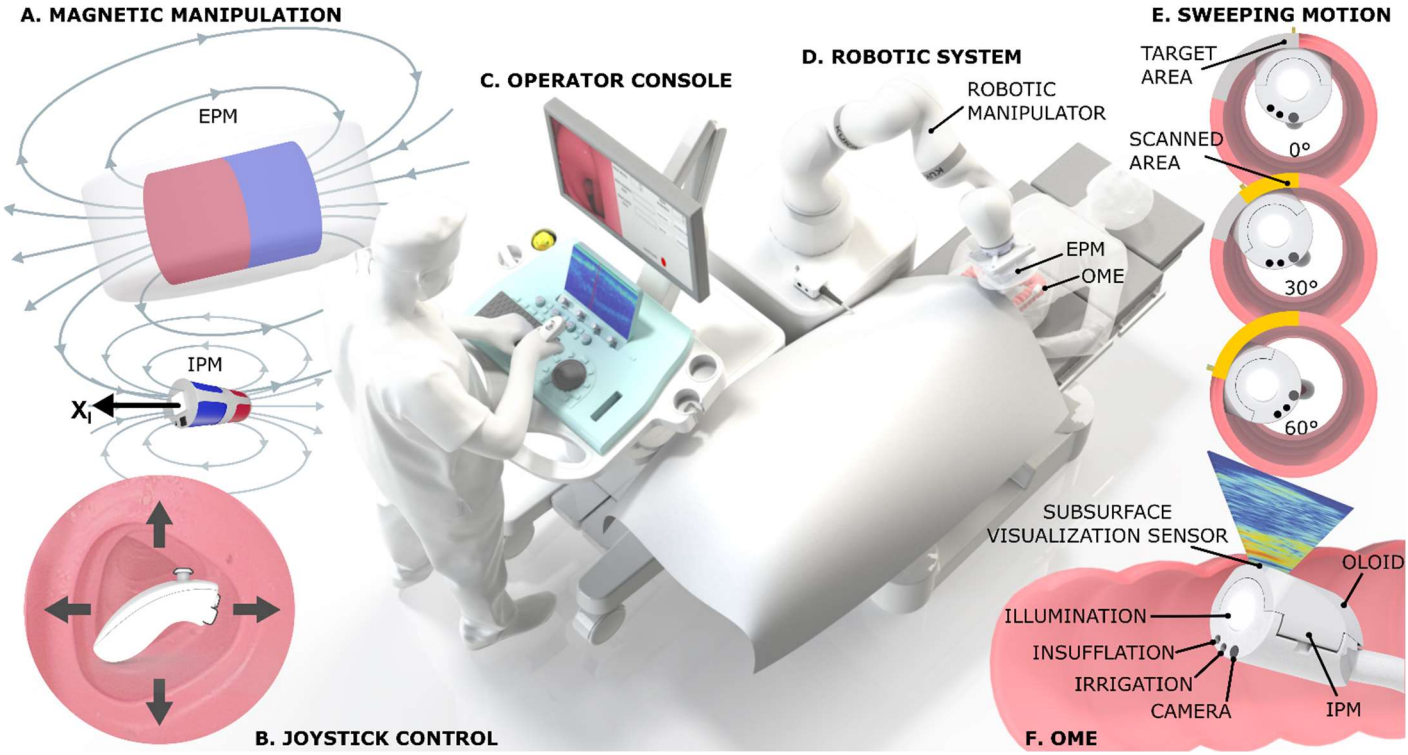

Figure 1: Oloid-shaped Magnetic Endoscope (OME) for recovering a lost DoF in magnetic medical robots, enabling virtual biopsies during endoscopy. (**A**) The magnetic manipulation system relies on the use of cylindrical permanent magnets where the field generated by the External Permanent Magnet (EPM) pulls and orients the Internal Permanent Magnet (IPM) during the procedure. The lost DoF ("roll") in magnetic manipulation around a magnet's magnetization axis ($\mathbf{X}_I$) is shown by the arrow on the IPM. (**B**) A joystick is used to control the robotic system where the operator only has to consider the desired direction based on the camera frame. (**C**) The operator console is used to visualize the camera feed for navigation and to inspect the 3D reconstructed virtual biopsies. (**D**) The robotic system, which includes a robotic manipulator, is used to manipulate the EPM and therefore the magnetic field to control the OME. (**E**) The sweeping motion is used to demonstrate the clinical viability of recovering the rolling motion for diagnostic sweeps. (**F**) The OME with the subsurface micro-ultrasound visualization sensor. See Movie S1 for a visual representation of the concept overview.

At the cutting edge of GastroIntestinal (GI) endoscopic technology is the concept of virtual biopsies where high-fidelity diagnostic sensors are used to perform in situ histopathology. In the context of GI cancer screening, where early and accurate detection is critical (*21*), the ability to perform virtual biopsies could eliminate the delays, costs, and complications associated with traditional histological analysis, allowing screening, diagnosis, and therapy to occur in a single procedure (*22*). A modality used alongside standard flexible endoscope is micro-ultrasound (μUS) or high-frequency US, typically delivered via mini-probe endoscopic ultrasound systems like the 20 MHz UM-3R (Olympus America Inc.), that are passed through the flexible endoscope's working channel. While effective for in situ cancer staging (*23*), positioning these probes precisely is essential to produce artifact-free imaging (*24*) which can be difficult in manual manipulation. Additionally, using a μUS probe occupies the working channel, limiting its use for tasks such as margin assessment during therapeutic procedures where access to the working channel is required for other purposes. Another example of GI μUS is transrectal μUS, such as the ExactVu™ probe (*25*) which can perform 29 MHz μUS of the prostate and has been externally controlled robotically to create 3D μUS images (*26*). However, these probes are specifically designed for rectal imaging and cannot reach deep within the GI tract, resulting in an unmet need.

Previous research on MFEs integrated a single μUS transducer capable of capturing histologically relevant images of the colon wall (*3*). However, the absence of roll control limited its ability to target specific areas, restore contact if misaligned, or perform radial sweeping motions. Designing 360° curved arrays presents substantial manufacturing challenges, as bending delicate thin transducer elements often leads to high failure rates (*27*). Some approaches introduce motors to rotate sensors (*28*); however, these compromise the simplicity and safety of magnetic manipulation, increase power consumption, and fail to address the overall dexterity of magnetic medical robots. These challenges underscore the need for enhanced dexterity in a clinically applicable manner, without additional actuation modes.

Inspired by embodied intelligence and the geometry of developable rollers, this work introduces a clinically applicable approach for generating torque around the magnetization axis in magnetic medical robots. This is achieved by geometrically coupling the existing two DoFs magnetic torque using just five magnetic control inputs for roll control, while still maintaining independent control over the original two DoFs. Developable rollers, observed in applications such as classical and quantum optics *(29)*, sphericon-shaped magnetic milli-robots *(30)*, and fluid mixing are known for their unique meandering rolling motions (Figure 2B). This innovation specifically leverages the oloid shape to achieve axial rotation, utilizing its axial asymmetry and interaction with the environment (see Movie S1). This method, demonstrated on the MFE platform, is agnostic to how the controlling magnetic field is generated, extending roll recovery to any magnetic manipulation system with at least five magnetic control inputs, including electromagnetic coil systems.

To validate this approach, we developed and evaluated a differential geometry-based control model for source-agnostic magnetic manipulation of an Oloid-shaped Magnetic Device (OMD) on various clinically relevant surfaces. In line with its motivation in GI endoscopy, an Oloid-shaped Magnetic Endoscope (OME) was designed and its ability to perform rolling and sweeping motions alongside existing DoFs demonstrated. To enable virtual biopsies, a 32-element, 28 MHz μUS linear array (Figure 2C(iii)) was integrated to capture high-resolution subsurface images. Autonomous μUS sweeping and 3D subsurface image reconstruction were achieved using a custom coupling detection algorithm, validated through both in vitro and in vivo testing in a porcine model. Finally, the system's ability to provide clinicians with in-situ lesion margin and staging information was evaluated in vivo by performing virtual biopsies of an artificially introduced polyp.

RESULTS

The DoF Limitation in Magnetic Manipulation

Magnetic manipulation in medical robotics is simplified through the dipole model where magnets are represented as magnetic dipoles (see Figure 3). This simplification remains accurate as the distance between the controlling source and the robot generally exceeds two times the size of the internal magnet (*31*).

As shown in Figure 3B, a magnetic object (internal dipole) with magnetic moment, $\mathbf{m}_I \in \mathbb{R}^3(ampere \cdot square\ meter)$ placed in an external magnetic field $\mathbf{B}_E \in \mathbb{R}^3(tesla)$ experiences both an alignment torque $\boldsymbol{\tau}_m$ and gradient-induced force $\mathbf{F}_m$. These are generated by the external dipole to minimize the system's potential energy. Conventionally, the magnetization axis of a magnetic object aligns with its local coordinate frame such that $\mathbf{X_I}$ is parallel to $\mathbf{m}_I$. However**,** since magnetic alignment torque is defined by the cross product $\boldsymbol{\tau}_m = \mathbf{m}_I \times \mathbf{B}_E$, when $\mathbf{m}_I$ is parallel to $\mathbf{B}_E$, $\boldsymbol{\tau}_m = \mathbf{0}$. As a result, magnetic alignment torque can only be generated around axes perpendicular to $\mathbf{m}_I$, meaning it is not possible to generate magnetic alignment torque around an object's magnetization axis to control the roll angle (ϕ). A visual representation and practical demonstration of this phenomenon are provided in Movie S1 along with a detailed mathematical explanation in the Supplementary Discussion.

Related work has explored the use of magnetic force to produce off-axis rigid body torques to control roll around the object's magnetization axis. This is achieved by coupling force and torque control through the inclusion of multiple discrete magnets (8, 9, 32) or by using a single magnet with a non-uniform magnetization or anisotropic shape (10–13).

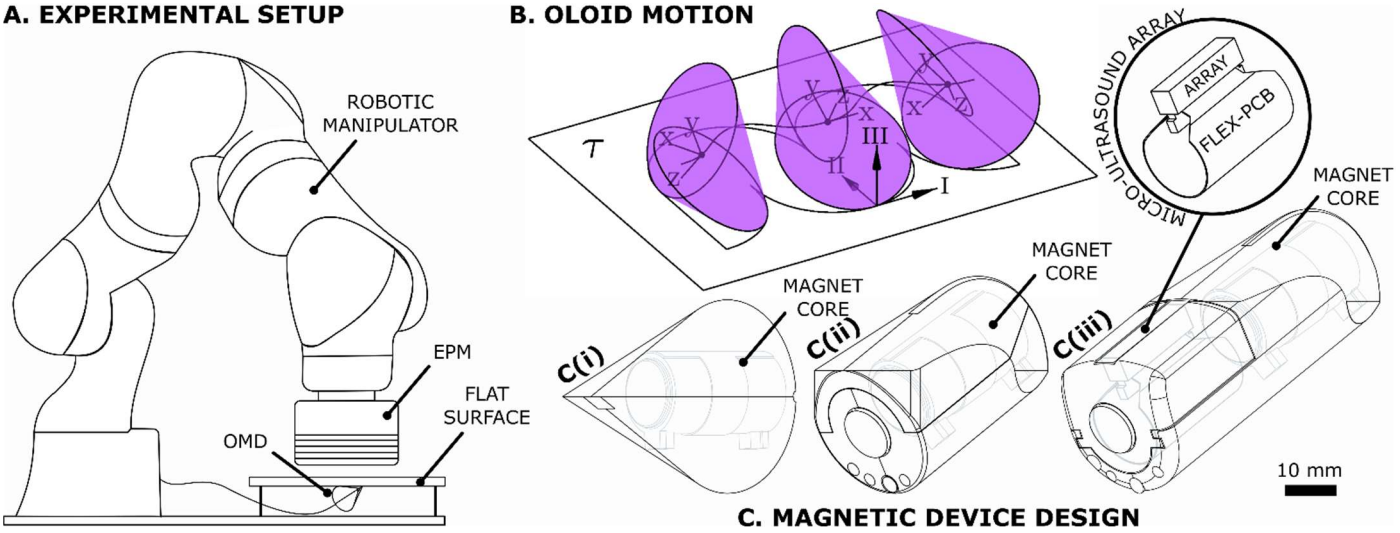

Figure 2: Experimental setup and design overview of the Oloid-shaped Magnetic Devices. (**A**) Benchtop experimental setup for the roll control experiments. (**B**) Illustration of the oloid shape rolling on a horizontal plane, *T* (based on Dirnbock et al. *(33)*) (**C(i)**) Oloid-shaped magnetic device, (**C(ii)**) Oloid-shaped magnetic endoscope and, (**C(iii)**) Oloid shaped magnetic endoscope with integrated micro-ultrasound array.

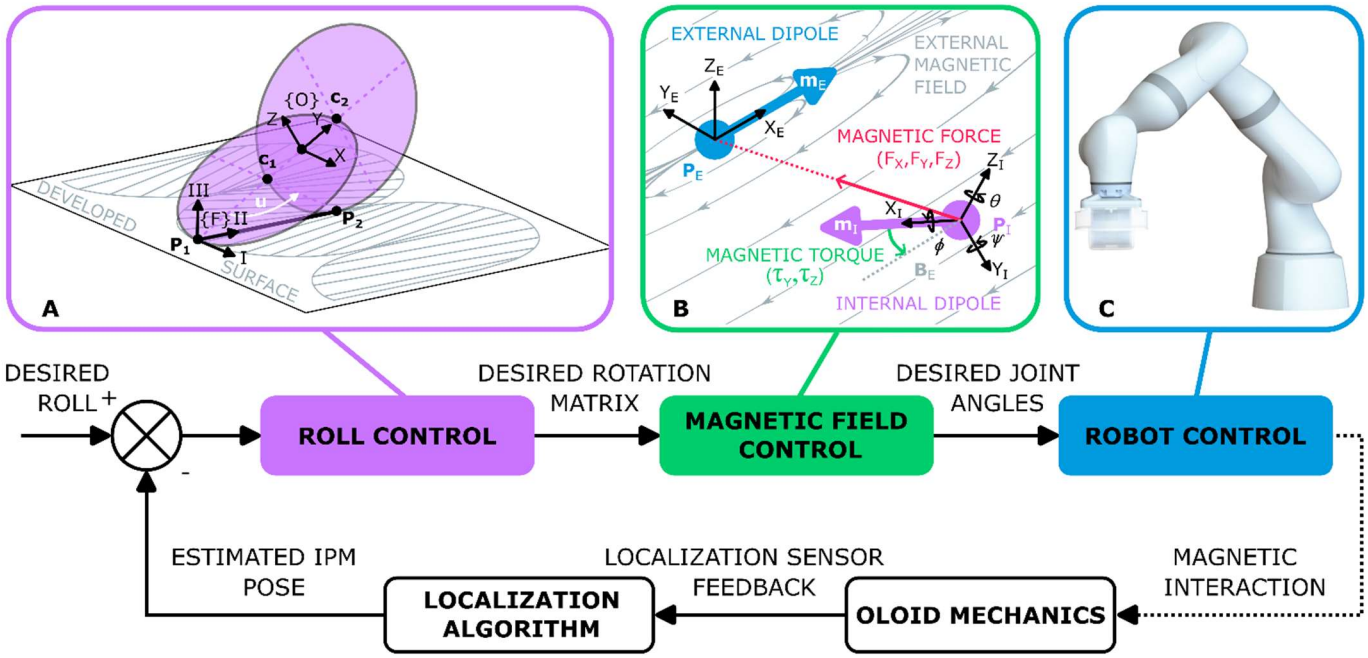

Figure 3: Block diagram control schematic for closed-loop control of the Oloid. (**A**) Roll control (purple): The differential geometry model of the oloid is illustrated according to *(33)* with (**X,Y,Z**) representing the local oloid coordinate frame {O} and (**I,II,III**) the fixed frame {F}. The developed surface corresponding to the projection of the oloid's generators is shown in grey. The centers of the oloid's defining circles are marked by $\mathbf{c}_1$ and $\mathbf{c}_2$ with contact points on the plane denoted by $\mathbf{P}_1$ and $\mathbf{P}_2$. (**B**) Magnetic field control: Shows the dipole-dipole model approximation where $\boldsymbol{p}_E$ and $\boldsymbol{p}_I$ are point dipoles and $\boldsymbol{m}_E$ and $\boldsymbol{m}_I$ represent the magnetic moments. Magnetic forces F_x, F_y and F_z and aligning torques τ_y and τ_z act on the internal dipole. Magnetic field lines represent the magnetic field $\mathbf{B}_E$ generated by the external dipole, which becomes uniform near the internal dipole. No torque τ_x is shown, as torque cannot be generated around the internal dipole's magnetization axis $\mathbf{X}_I$. (**C**) Robot control (blue): Single EPM system enabling precise magnetic field manipulation to control the Oloid's motion.

The Oloid

Coupling existing DoFs to regain roll control in magnetic manipulation required a geometry with axial asymmetry. For bi-directional rolling, the geometry also needed at least one plane of symmetry, allowing roll actions in two distinct, opposing directions.

The oloid, distinguished from others in the developable roller family, is formed by joining two perpendicular, equal intersecting circles with a distance between their centers ($\mathbf{c}_1$ and $\mathbf{c}_2$) equal to their radii (shown in Figure 3). This unique shape lacks vertices and maintains continuous surface contact during rolling due to its developable, flattenable (developed) surface (Figure 3). As a ruled surface, it is generated by straight lines (generators) connecting its circles at points $\mathbf{P}_1 \in \mathbb{R}^3$ and $\mathbf{P}_2 \in \mathbb{R}^3$, along a directrix. This leads to its parametric equation:

$$\mathbf{r}(u,v) = \mathbf{P}_1(u) + v(\mathbf{P}_2(u) - \mathbf{P}_1(u)) \quad (1)$$
$$\text{where } \frac{-2\pi}{3} \le u \le \frac{2\pi}{3},\ 0 \le v \le 1$$

The script to generate the 3D surface of the oloid using Equation 1 has been made available in our accompanying Data repository.

When an oloid rolls on a flat plane, one generator line contacts the plane becoming the instantaneous axis of rotation, with angular velocity, $\boldsymbol{\omega} \in \mathbb{R}^3$ (rad/s), parallel to this line and tangent to the plane, expressed as:

$$\boldsymbol{\omega} \parallel \mathbf{P}_2 - \mathbf{P}_1 \Rightarrow \boldsymbol{\omega} \times (\mathbf{P}_2 - \mathbf{P}_1) = \mathbf{0} \quad (2)$$

To control rotation around a robot's magnetization axis using geometric misalignment and two DoFs magnetic torque, the magnetization axis must not be parallel to the object's angular velocity.

This exists in the oloid over the controllable range, in direct contrast with a shape like the cylinder where its angular velocity is always parallel to its central axis. See "Roll Generation in the Oloid" in the Supplementary Discussion for further details.

OME versus MFE DoFs

To embody the unique rolling abilities of the oloid into the OME design (Figure 2C(ii)), its pure form was adapted to meet clinical requirements and to incorporate essential endoscope features. This required evaluating the oloid's functional areas and their relation to the range of roll motion. By merging the key elements of the oloid with the cylindrical MFE, a hybrid design was achieved that adhered to clinical size constraints, as detailed in "Oloid Shape Integration" in Materials and Methods.

Dexterity was assessed through a direct comparison between the MFE which has a cylindrical shape and the

OME, evaluating their ability to perform independent tilt and yaw motions, as well as coupled rolling motion (see "Magnetic Actuation of the Endoscope" in Materials and Methods for details). These experiments were conducted on lubricated Perspex using the MFE's robotic system as illustrated in Figure 2A.

As shown in Figure 4 and Movie S2, the OME not only enabled controlled rolling motion—albeit coupled with tilt and yaw—but also allowed for more independent tilt and yaw control compared to the MFE's cylindrical design. The MFE experienced uncontrollable roll during manipulation, minimized in past designs through offset IPM placement for corrective torque and minimal-energy orientation. In GI endoscopy, due to its tubular nature, tilt and yaw are the primary DoFs, with roll desired only for specific tasks like tissue scanning or tool or camera manipulation. See Figure S2 in Supplementary Figures for *x, y* translational experiments and the orientation-time graphs used to generate the radar plots in Figure 4.

Generating Rolling Motion with the Oloid in Open-Loop

To control the oloid's rolling motion, we used an analytical differential geometry model detailed in "The Oloid Model" in Materials and Methods. This model defined the line of contact during rolling and calculated the corresponding transformation matrix for the oloid's local coordinate frame. We hypothesized that adjusting the applied magnetic field according to this sequence would replicate the desired rolling motion in an OMD in open-loop. We developed an OMD (Figure 2C(i)) with a 3D-printed oloid-shaped shell (20 mm radius, 60 mm length) that accommodated an IPM with integrated localization. This localization data tracked the roll and compared it to the model's predictions. Assuming perfect magnetic coupling, the EPM was programmed to follow the transformation matrix sequence. Initial tests on a high-friction silicone substrate (Figure 5A and Movie S3) emulated the model's non-slip condition. Tests were repeated on bumpy foam, flat foam, and Perspex (Figures 5B-D and Movie S3) to evaluate performance across different surfaces over a 180° range (see Figure S3 for extended results). The silicone surface closely matched the model's non-slip condition, showing the highest correlation with predicted motion, while Perspex, which was unable to maintain the non-slip condition, showed the least correlation. A scaled-down demonstration was performed in an electromagnetic coil with a mini-OMD (Figure S4) to assess the model's versatility and scalability.

These results indicate that although this open-loop setup can achieve rolling motions in a range of conditions, a closed-loop control system was crucial for precise control, particularly when environmental conditions differed from model assumptions.

Closed-Loop Control of the Oloid

In real-world medical settings, magnetic coupling cannot be reliably assumed, necessitating device localization. Additionally, manufacturing imperfections and environmental factors lead to deviations from the model, prompting the development of a differential geometry-based closed-loop control system for the oloid (detailed in Materials and Methods). Here the oloid's closed-loop controllability and therefore its potential for innovation in medical devices was evaluated. The OMD was tested on surfaces simulating

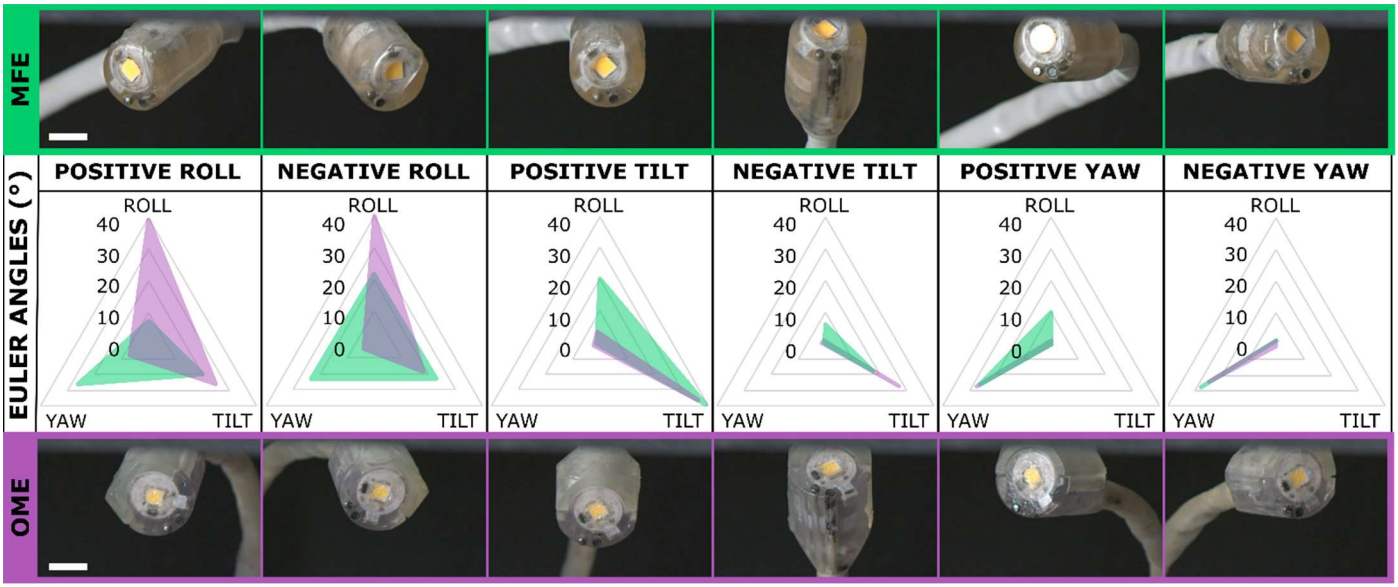

Figure 4: Comparison of 3-DoF orientation control between the Oloid Magnetic Endoscope (OME) and the Magnetic Flexible Endoscope (MFE). The figure illustrates the coupling between positive and negative roll, tilt, and yaw for the MFE (green) and OME (purple). Radar plots for each DoF display the average absolute deviations in roll, tilt, and yaw (measured in degrees) across three repetitions (Figure S2). The scale bars represent 10 mm. See Movie S2 for related multimedia.

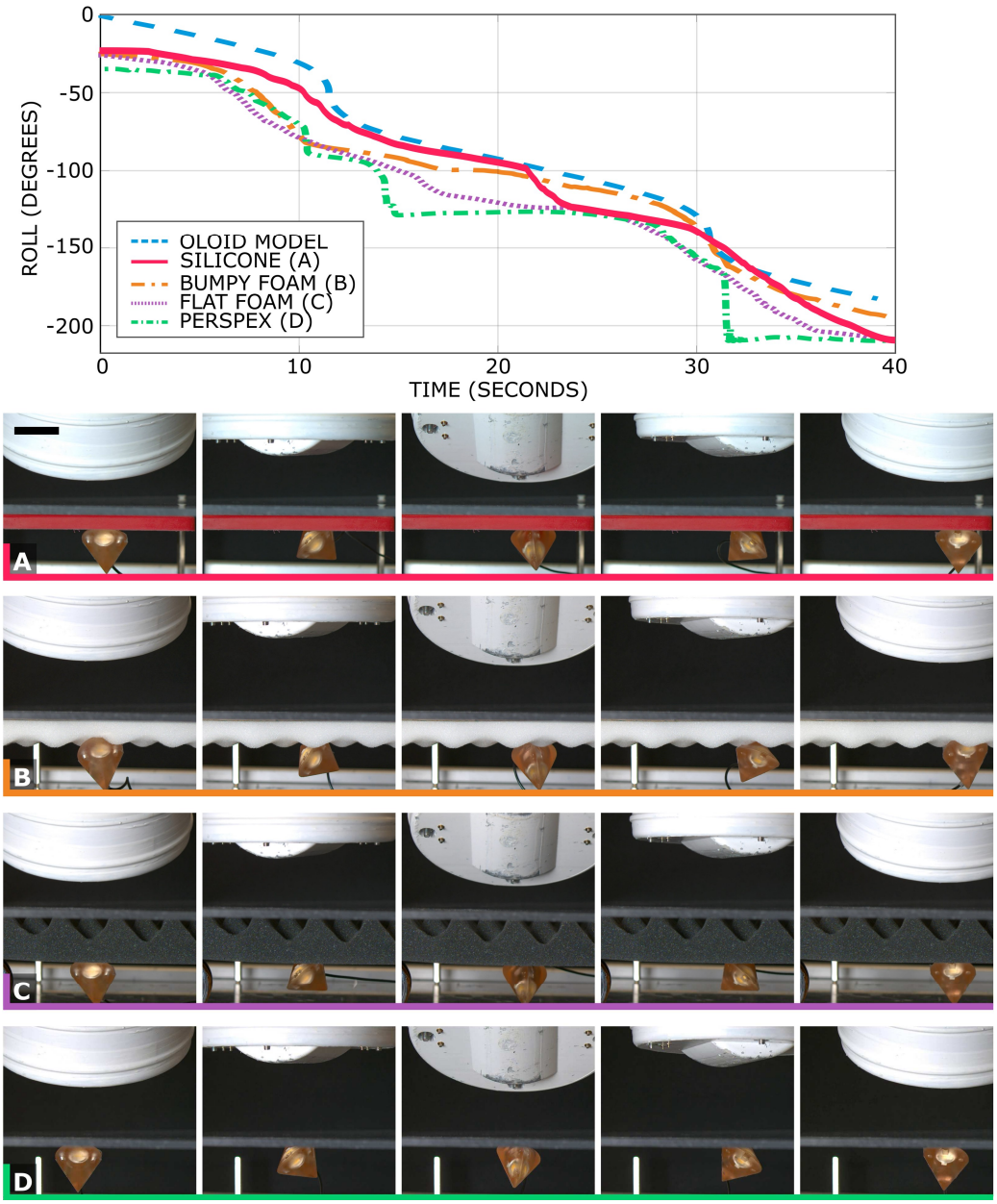

Figure 5: Open-loop control of the Oloid-shaped Magnetic Device (OMD) on various surfaces. The oloid's rolling behavior on (**A**) silicone, (**B**) bumpy foam, (**C**) flat foam and (**D**) Perspex, compared to the predicted roll from the oloid model. Each snapshot shows the EPM position and orientation for reference. The scale bars represent 30 mm. See Movie S3 for related multimedia

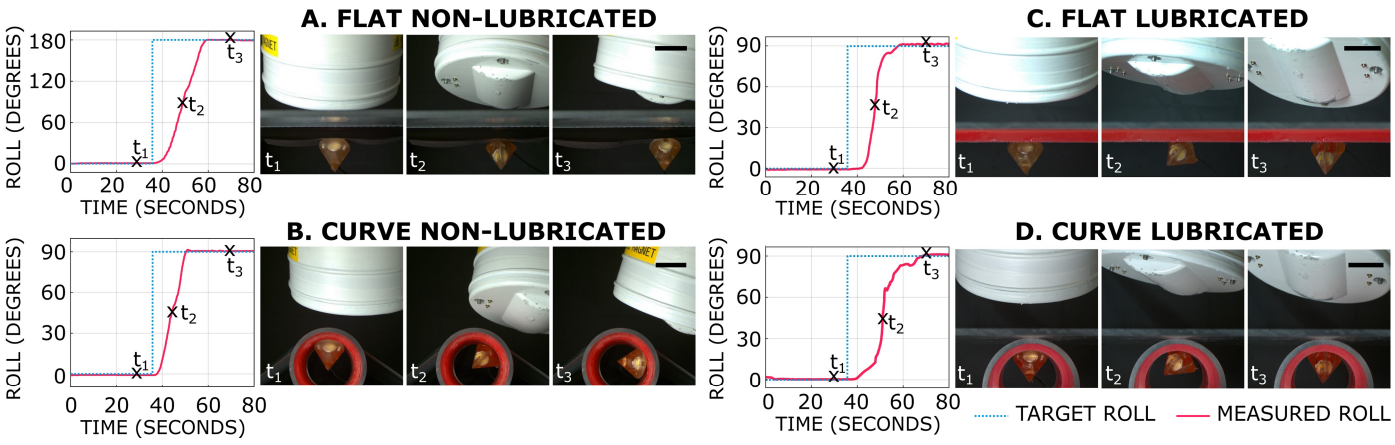

Figure 6: Closed-loop control of the Oloid-shaped Magnetic Device (OMD) with step input on various surfaces. Rolling performance is shown on (**A**) a flat, non-lubricated surface, (**B**) a curved, non-lubricated surface, (**C**) a flat, lubricated surface, (**D**) a curved, lubricated surface. Snapshots at times t_1, t_2, and t_3 progress from left to right. The scale bars represent 30 mm. See Movie S4 for related multimedia.

the internal GI tract structures, such as mucus-lubricated curved (colon, esophagus) and flat (stomach) surfaces.

Initial tests on a non-lubricated flat surface established a performance baseline (Figure 6A). Subsequently, more complex conditions were introduced, including lubricated (Figure 6C & D) and curved surfaces (Figure 6B & D). On the initial flat surface, a 0° to 180° step function input demonstrated a full range of motion. For lubricated and curved surfaces, a 0° to 90° step function input was applied. The results, exhibited in Figure 6 (see Figure S5 for extended results) and Movie S4, highlight the system's adaptability and precise control across all test conditions. The lubricated surfaces enabled the oloid's ability to decouple roll from translation and generate pseudo-on-axis roll effectively.

In vivo Rolling and Sweeping Motions

For a practical in vivo demonstration of the system's clinical relevance, we selected a porcine model due to the similarity of porcine and human GI anatomy. The primary goal of the in vivo trials was to validate the OME's ability to perform controlled rolling and sweeping motions in realistic conditions of friction and tissue interaction.

Two distinct experiments were designed to support these capabilities: one to observe the OME's sweeping motion across the top half of the lumen of the colon and the other to assess its pure rolling motion within a ±50° range. The results, displayed in Figure 7 and Movie S5, include snapshots from a separate standard endoscope camera (see Figure S8) capturing the sweeping and rolling motions of the OME. Notably, the sweeping motion, which combined horizontal translation and roll motion to produce an arch-like effect, achieved a range of ±60°. This combined motion enabled radial scanning by the sensor, with rolling adjusting the probe's orientation and translation moving the endoscope across the surface.

Pre-clinical Validation – Virtual Biopsy 3D Reconstruction

The primary motivation of this work was to enable virtual biopsies in MFEs, to enhance diagnostic capabilities beyond those of standard flexible endoscopes. Virtual biopsies allow for detailed tissue analysis, such as assessing lesion malignancy and margins, without the need for physical biopsies.

The OME is sensor-agnostic, however, for demonstration purposes, we integrated a 32-element 28 MHz μUS array called the OME-U (see the "Ultrasound Integration" section). By combining our autonomous sweeping algorithm (see the "Autonomous Sweeping" section) with precise six DoF localization, the system generated comprehensive μUS imaging datasets. These datasets integrated high-quality 2D ultrasound images with positional data, allowing for the creation of high-fidelity 3D reconstructions of target areas. This process is outlined in the "3D Reconstruction" section.

Preliminary validation was conducted on a benchtop setup with a silicone phantom and the OME-U (Figure 2C(iii)). The phantom included copper bands as echogenic subsurface targets. Signals were accurately captured and reconstructed, confirming system precision (see Figures S6, S7 and Supplementary Methods).Further validation was conducted in vivo by performing an autonomous sweep over healthy tissue followed by a simulated flat polyp in the same region of the porcine colon, created by injecting submucosal lifting agent (see Figure 8A and Movie S6).

The 3D reconstructed volumes were visualized dynamically using MATLAB (Figure 8C and Movie S6), allowing operators to rotate, translate, and zoom. An isosurface representation feature enabled detailed inspection of tissue features (Figure 8D) through customizable visibility thresholds (see "3D Reconstruction").

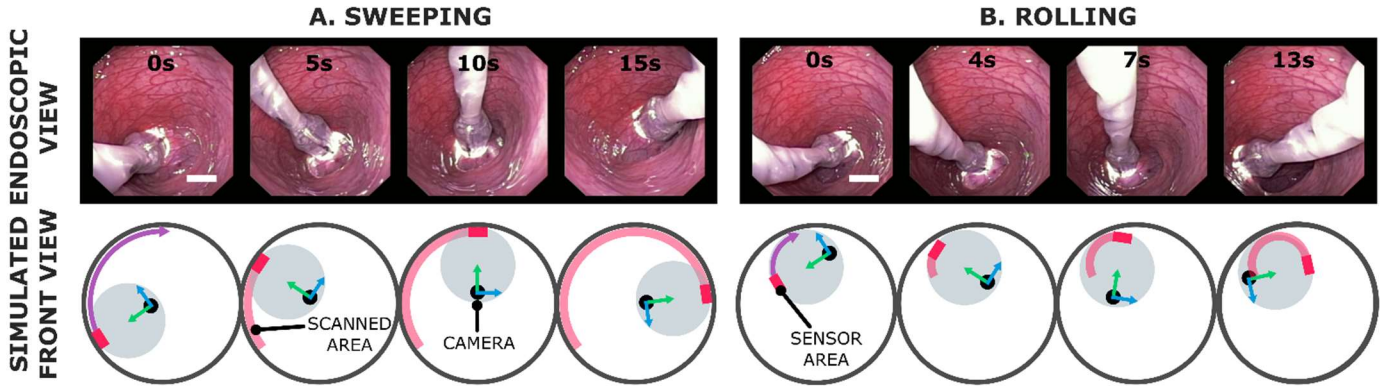

Figure 7: In vivo sweeping and rolling of the Oloid Magnetic Endoscope (OME). Selected views from the standard endoscope camera and mirrored simulated front views show the motion of the OME's sensor area and camera during (**A**) sweeping and (**B**) rolling motions. The black circle with blue and green arrows represents the OME's onboard camera and its frame, while the purple arrow indicates the planned motion of the sensor area. The scale bars represent 20 mm. See Movie S5 for related multimedia.

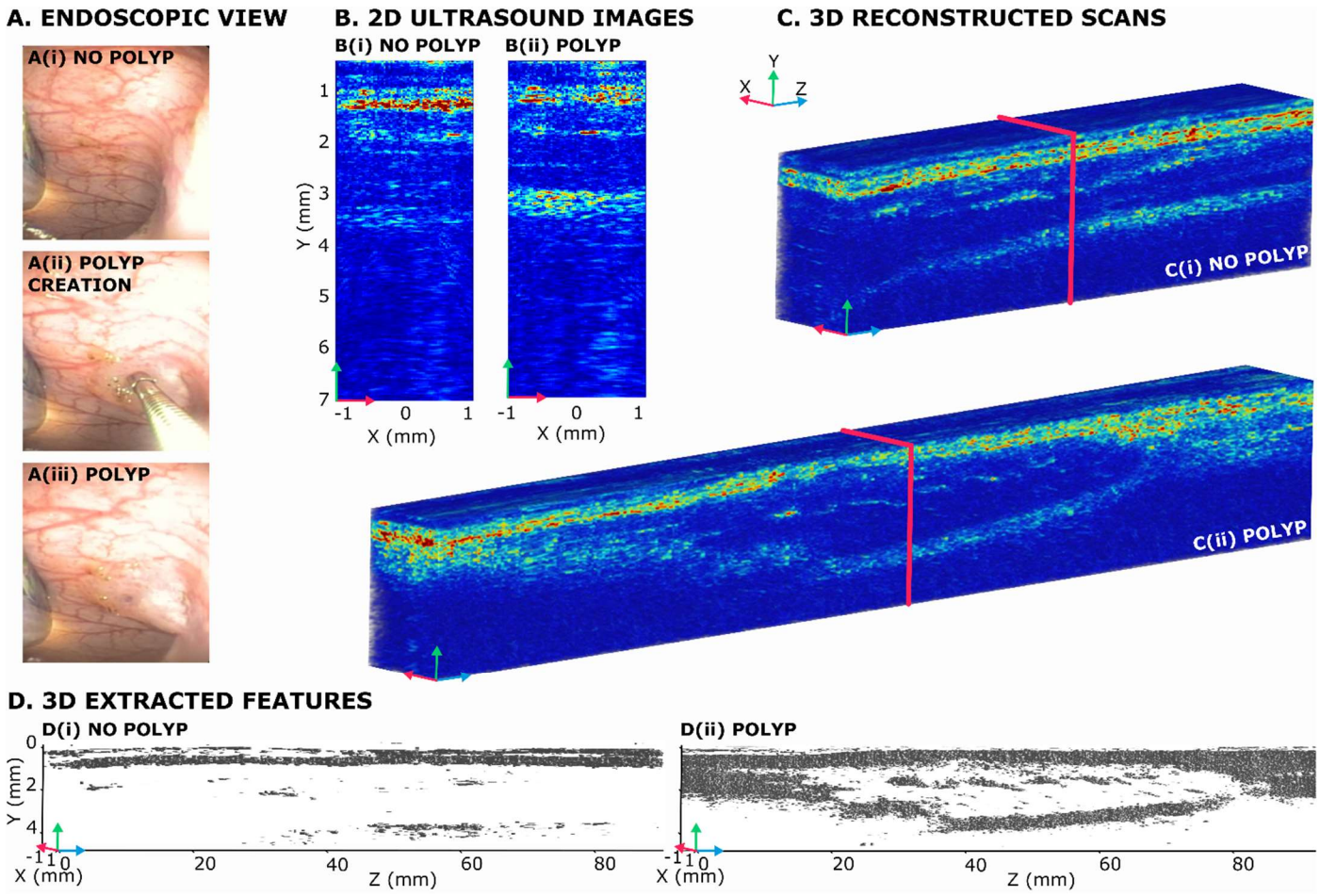

Figure 8: In vivo subsurface 3D reconstruction of micro-ultrasound images for achieving virtual biopsies with the Oloid Magnetic Endoscope (OME). (**A**) Endoscopic view showing stages 1-3 of polyp creation. (**B**) 2D Ultrasound images: (**B(i)**) without polyp and (**B(ii)**) with polyp, (**C**) 3D Reconstruction of the ultrasound scans: (**C(i)**) without polyp and (**C(ii)**) with polyp, with the red square indicating the position of the 2D images (**B(i)**) and (**B(ii)**) within the 3D scan. (**D**) 3D Isosurface rendering highlights extracted features of interest: (**D(i)**) without polyp and (**D(ii)**) with polyp. See Movie S6 for related multimedia.

This was particularly effective in visualizing the flat polyp structure within the 3D volume (Figure 8D(ii)), showcasing the diagnostic potential of the approach. While elements at depth can be observed even in the no polyp case, these features are less intense and inconsistent, whereas the polyp case shows a discontinuity in two layers that meet at both ends.
The accuracy of the 3D reconstruction was assessed by comparing the reconstructed volume of the polyp against the injected volume, showing a 9.6% overestimation (injected volume: 1 ml, reconstructed volume: 1.106 ml).

DISCUSSION

This work introduces an approach to closed-loop roll control in magnetic medical devices, particularly MFEs, using an oloid-shaped design. This shape provides additional dexterity, enabling controlled rolling without additional power consumption or actuation modes, ideal for endoscopes including untethered capsule endoscopes. A precise closed-loop control scheme that integrates MFE localization was developed, addressing scenarios where perfect magnetic coupling cannot be assumed. Roll control was effectively demonstrated in benchtop trials and subsequently in in vivo trials.

This study has demonstrated the approach across different scales (OMD, OME, and mini OMD) and control sources (single EPM and electromagnetic coil system), in both tethered and untethered configurations. Although our differential geometry-based model provides a framework for broad clinical applications using any magnetic field source with at least five magnetic control inputs, comprehensive parametric studies are needed to validate utility in other applications. For example, extending this approach to more dynamic surfaces than the colon will require real-time model parameter estimation.

The design and in vivo testing of the OME within the colon demonstrated the capacity of the oloid to be integrated into a device that met the specific design requirements for colonoscopy achieving safe rolling motion and an application-specific sweeping motion. Our results also demonstrated that the OME could roll, tilt, and yaw with greater independence and stability

than cylindrical MFEs, which do not have active roll control.

Previous work (*3*) was confined to 2D scans using single-element transducers, as linear arrays were impractical due to the absence of roll control. By leveraging roll control, our approach enabled robotically controlled, autonomous sweeping to create 3D μUS images with deeper anatomical reach than transrectal μUS. These virtual biopsies offer potential real-time diagnostic insights without requiring physical samples.

The OME's sensor-agnostic design supports the integration of various diagnostic or therapeutic modalities, such as Optical Coherence Tomography (*34*) or therapeutic lasers (*35*), making it adaptable for future applications. In addition, roll control could facilitate precise interventions like submucosal dissection, and targeted ultrasound-triggered drug delivery (*36*, *37*).

The oloid-based roll control system and autonomous virtual biopsies contribute to the expanding autonomy of MFEs, which includes autonomous navigation (*38*), polyp detection, and shared control physical biopsy tasks (*20*). These advancements could allow endoscopists to focus on critical diagnostic and therapeutic decisions while autonomous systems handle routine navigation and tasks (*39*). This could also reduce the training times for endoscopists and potentially allow multiple procedures to be supervised simultaneously.

The single EPM system of the MFE has been validated in human trials with patients of normal Body Mass Index (BMI) (*19*), however, patients with higher BMI pose challenges due to increased EPM-IPM distances, reducing magnetic force and torque. Increasing the EPM size to generate stronger magnetic fields, can potentially address these limitations. Additionally, the current single EPM system limits vertical (z-axis) control, causing the endoscope to remain in constant contact with the top half of the lumen of the colon. To extend the sweeping range to include the lower half, patient repositioning is required. This design approach is consistent with standard clinical practice, where patient repositioning is a method for ensuring comprehensive colon examination (*40*). However, implementing more complex field generation systems (*1*, *14–16*) would enable full 360° scanning in scenarios where patient repositioning is not possible. Rolling demonstrations with the electromagnetic coil system revealed this potential, showing successful oloid movement across lower surfaces.

Furthermore, the OME's enhanced dexterity and diagnostic capabilities have the potential to address gender disparities in colonoscopies, as standard flexible endoscope procedures tend to be more challenging in women, leading to higher rates of incomplete procedures and lower adenoma detection rates (*41*). In conclusion, the oloid shape facilitates clinically applicable torque generation around the magnetization axis in magnetic medical robots, enhancing the dexterity, diagnostic capabilities, and autonomy of MFEs and magnetic medical robots overall. This approach sets the stage for more autonomous and efficient medical procedures deep within the anatomy. With ongoing clinical validation, such advancements have the potential to transform minimally invasive diagnostics and treatments, making them more accessible and effective for a broader range of patients.

MATERIALS AND METHODS

The Oloid Model

For the successful control of magnetically manipulated oloid-shaped devices, a deep understanding of the oloid's motion was crucial. Although previous studies have modeled the behavior of the oloid—or "two-circle roller"—on flat surfaces (*33*, *42*, *43*), our work is based on an adaptation of the differential geometry framework by Dirnbock et al. (*33*) where full derivations can be found. In this work, the application of the previous model was extended to curved and lubricated surfaces for any defining oloid radius, r.

We assign a fixed coordinate frame $\{\mathrm{F}\}$ with orthonormal vectors $\mathbf{I}, \mathbf{II}, \mathbf{III} \in \mathbb{R}^3$ on the plane for the initial position and orientation of the oloid. As the oloid moves along the plane, its motion can be parametrized by the arc length $u\ (radian)$ of the contact point, $\mathbf{P}_1$, on the edge of one of its circles over the region:

$$u \in \left(-\frac{2\pi}{3}, 0\right) \cup \left(0, \frac{2\pi}{3}\right) \tag{3}$$

If $\{\mathrm{O}\}$ denotes the coordinate frame with orthonormal vectors $\mathbf{x}, \mathbf{y}, \mathbf{z} \in \mathbb{R}^3$ at the geometric center of the oloid, then the homogeneous transformation matrix of $\{\mathrm{O}\}$ with respect to $\{\mathrm{F}\}$ is:

$$\mathbf{T}_F^{\mathrm{O}} = \begin{bmatrix} \mathbf{R}_F^{\mathrm{O}} & \mathbf{t}_F^{\mathrm{O}} \\ \mathbf{0} & 1 \end{bmatrix} \in SE\,(3) \tag{4}$$

where, using $s = \sin(u)$ and $c = \cos(u)$ for brevity:

$$\mathbf{t}_F^{\mathrm{O}} = \frac{r\sqrt{3}}{9} \begin{bmatrix} \frac{cs\sqrt{1+2c}}{2(1+c)\sqrt{2(1+c)}} + \mathrm{sign}(u)\arccos(u)\frac{c\sqrt{2}}{\sqrt{1+c}} \\ \frac{15+13c-c^2}{2(1+c)} + \ln\left(\frac{2}{1+c}\right) \\ \frac{3\sqrt{3}(2+c)}{2\sqrt{2(1+c)}} \end{bmatrix} \in \mathbb{R}^3 \tag{5}$$

is the translation vector and:

$$\mathbf{R}_p^0 = \frac{\sqrt{3}}{9}\begin{bmatrix} \frac{(5+c)\sqrt{1+2c}}{\sqrt{2(1+c)}} & \frac{(2+c)s\sqrt{1+2c}}{(1+c)\sqrt{2(1+c)}} & \frac{(5+4c)s}{(1+c)\sqrt{2(1+c)}} \\ \frac{(c-1)s}{1+c} & \frac{5+5c-c^2}{1+c} & -\frac{(1+2c)\sqrt{1+2c}}{1+c} \\ -\frac{3s\sqrt{3}}{\sqrt{2(1+c)}} & \frac{3c\sqrt{3}}{\sqrt{2(1+c)}} & \frac{3\sqrt{3(1+2c)}}{\sqrt{2(1+c)}} \end{bmatrix} \in SO(3) \quad (6)$$

is the rotation matrix.

The model assumes that the oloid undergoes pure, no-slip rolling on a perfectly horizontal surface. Additionally, its center of mass aligns with its geometric center and its overall rolling direction remains fixed in the initial reference frame.

These assumptions demonstrate that while the pure oloid model captures rolling on flat, high-friction surfaces, modifications were required for curved and lubricated environments.

To adapt the model for non-planar surfaces and to select rolling direction, we introduced a rolling surface element, $\mathbf{R}_S \in SO(3)$, and a rolling direction element, $\mathbf{R}_D \in SO$ with respect to $\{\mathrm{F}\}$. $\mathbf{R}_S$ rotates the model in **II** to account for changes in the angle of the surface normal as the oloid rolls on non-planar surfaces and $\mathbf{R}_D$ adjusts for the desired rolling direction in **III**.

For curved cylindrical surfaces, adjustments were calculated based on the surface's approximate radius, $r_c\ (meters)$. The translation in **I** (Figure 2B) of the oloid's center of mass, $\mathbf{s}(u) \in \mathbb{R}^3$, was used in the arc length equation to derive the angle of the surface normal, $\boldsymbol{\theta}(u)$, relative to the horizontal, as a function of u.

$$\boldsymbol{\theta}(u) = \mathbf{s}(u)/r_c \quad (7)$$

$\boldsymbol{\theta}(u)$ was then used to define $\mathbf{R}_s$ for every u.

This adjustment was only necessary on non-lubricated surfaces since lubricated surfaces characterized by stick-slip motion (*44*), remove the pure no-slip constraint, decoupling translation from rotation. For lubricated surfaces, the control system used the unaltered rotation matrix for orientation and original control for x and y translation. In open-loop, the full unaltered transformation matrix assumed the no-slip condition. For closed-loop, this condition was assumed only in non-lubricated cases, with adjustments applied for curved surfaces using pre-measured parameters ($\mathrm{r_c}$). In both lubricated cases, the system utilized the unaltered rotation matrix exclusively, omitting translation to maintain a central position and demonstrate pseudo on-axis roll. The MATLAB scripts for this model have been made available in our accompanying Data repository.

Roll Closed-Loop Control

To control the rolling motion of the OMD in a closed-loop system, we leveraged the closure and inverse property of the SO group to denote the rotation matrix error as follows:

$$\mathbf{E} = \mathbf{R}_d\mathbf{R}^{\mathrm{T}} = \mathrm{e}^{\mathrm{S}(\boldsymbol{\varepsilon})} \in SO(3) \quad (8)$$

where $S(\boldsymbol{\varepsilon}) \in \mathfrak{so}(3)$ is the Lie algebra of $\boldsymbol{E}$ (a skew-symmetric matrix). Here, $\hat{\boldsymbol{\varepsilon}} = \frac{\boldsymbol{\varepsilon}}{\|\boldsymbol{\varepsilon}\|} \in \mathbb{R}^3$ is the axis of rotation error, and $\| \boldsymbol{\varepsilon} \|$ is the magnitude of the rotation error in radians. Taking the time derivative of the error, we obtained:

$$\dot{\mathbf{E}} = S(\dot{\boldsymbol{\varepsilon}})\mathbf{E}, \dot{\boldsymbol{\varepsilon}} = \boldsymbol{\omega}_d - \boldsymbol{\omega} \quad (9)$$

From this, we denote the input angular velocity as:

$$\boldsymbol{\omega} \triangleq \boldsymbol{\omega}_d + \mathbf{K}_1\boldsymbol{\varepsilon} \quad (10)$$

where $\mathbf{K}_1 \in \mathbb{R}^{3\times3}$ is a positive-definite gain matrix. This formulation ensured that errors decay exponentially over time:

$$\dot{\boldsymbol{\varepsilon}} = -\mathbf{K}_1\boldsymbol{\varepsilon} \longrightarrow \boldsymbol{\varepsilon}(t) = \mathrm{e}^{-\mathrm{K}_1\boldsymbol{\varepsilon}t}\boldsymbol{\varepsilon}_0 \quad (11)$$

with $\boldsymbol{\varepsilon}_0$ is the initial error at $t = 0$. The setup guaranteed that the error decays exponentially:

$$\lim_{\mathrm{t}\to\infty} \boldsymbol{\varepsilon}(t) = \mathbf{0} \quad (12)$$

At $\boldsymbol{\varepsilon} = \mathbf{0}$, we have $\mathrm{e}^{\mathrm{S}(0)} = \mathbf{I}$, meaning that $\mathbf{R} = \mathbf{R}_d$, which aligns the desired and actual orientations. Finally, the torque variation is set proportional to velocity. For $\boldsymbol{\omega}_d = \mathbf{0}$, the equation simplifies to:

$$\delta\boldsymbol{\tau} = \mathbf{K}_2\boldsymbol{\omega} = \underbrace{\mathbf{K}_2\mathbf{K}_1}_{\mathbf{K}}\boldsymbol{\varepsilon} \quad (13)$$

This desired torque variation served as the control input for the magnetic field system, enabling precise roll control as detailed in "Magnetic Actuation of the Endoscope". Through magnetic interactions and the mechanics of the oloid, the device's pose was adjusted, with continuous pose measurement via the IPM's localization system, completing the feedback loop. As illustrated in Figure 3, the roll control stage calculated the necessary torque adjustments. This information was fed into the magnetic field control, where a simple proportional controller managed orientation control. To enhance operational efficiency, a predefined lookup table of the oloid's differential geometry model was employed to eliminate the need to recompute transformation matrices at each step.

Robotic System Design

The system (Figure 2A) consisted of an EPM (cylindrical, axially magnetized, 101.6 mm in diameter and length,

NdFeB, N52 grade, KJ Magnetics) positioned at the end effector of a medical-grade, 7-DoF serial robotic manipulator (LBR Med R820, KUKA) which was used to steer a tethered magnetic device with an embedded Internal Permanent Magnet (IPM). Actuation was achieved by applying magnetic forces and torques to the IPM to modify its position and orientation by adjusting the pose of the EPM. Surrounding the IPM was a flexible circuit containing Hall Effect sensors and an Inertial Measurement Unit (IMU) for IPM localization. The data from the Hall effect and IMU sensors of the IPM, influenced by its current pose within the EPM's magnetic field, along with an additional non-actuating field generated by an electromagnetic coil surrounding the EPM, enabled real-time estimation of the magnetic device's pose at a frequency of 100 Hz (*44*). This feedback was crucial for implementing closed-loop control and automated tasks.

The user interface included a joystick to navigate the GI tract with the OME based on visual feedback from the embedded camera (Figure 1B). Diagnostic images were captured with the μUS array using a research array controller (Vantage HF 128, Versaonics) and post-processed using MATLAB (MathWorks, Inc.). The components were interfaced with the Robot Operating System (ROS) owing to the modularity and straightforward multi-threading capabilities of ROS.

Three magnetic devices were developed for this paper. The first was an OMD (Figure 2C(i)), used to validate a differential geometry-based closed loop control model for the oloid shape. The second was an OME (Figure 2C(ii)), utilized to demonstrate the clinical applicability of this approach. The third was an adapted version of the OME, which included a μUS array (OME-U) (Figure 2C(iii)). A design-specific localization calibration process (see Supplementary Methods) was implemented to mitigate the effect of any manufacturing imperfections in each of these designs.

Magnetic Actuation of the Endoscope

The control of the endoscope pose was split into two separate subsystems, one dedicated to the orientation control, and another one dedicated to the position control. Due to the inherent nonlinearities of the field $\mathbf{B}_E$, the global relation between EPM motions and torques/forces is nonlinear. Given the local nature of the movements and the low velocity of the robot and the endoscope, the control approach adopted was linearized. The validity of the models and control action were therefore only local, commanded movements must be small and the boundary conditions needed to be computed at every time step.

Orientation control was achieved locally by converting the desired torque variation ($\delta\boldsymbol{\tau}$) into the desired motion of the EPM. In the case of roll control, $\delta\boldsymbol{\tau}$ was an output of the roll control stage. For tilt and yaw, $\delta\boldsymbol{\tau}$ was simply the desired change in τ_y and τ_z, respectively. Using the magnetic dipole model and Maxwell's force/torque equations (see Supplementary Discussion), we defined a magnetic Jacobian that relates the positions and orientations of the IPM and EPM to the forces and torques applied to the IPM, assuming a constant pose of the IPM:

$$\begin{bmatrix}\boldsymbol{\delta f}_{lin}\\ \boldsymbol{\delta\tau}_{lin}\end{bmatrix} = \boldsymbol{J}_F(\boldsymbol{p}_E, \boldsymbol{p}_I, \widehat{\boldsymbol{m}_E}, \widehat{\boldsymbol{m}_I}) \begin{bmatrix}\boldsymbol{\delta p}_E\\ \boldsymbol{\delta}\widehat{\boldsymbol{m}_E}\end{bmatrix} \quad (14)$$

where $\mathbf{p}_E$, $\mathbf{p}_I \in \mathbb{R}^3$ are the positions of the EPM and IPM (Figure 3), $\widehat{\mathbf{m}_E}$ and $\widehat{\mathbf{m}_I} \in \mathbb{R}^3$ are their orientations, and $\delta\mathbf{F}_{lin}$, $\delta\boldsymbol{\tau}_{lin} \in \mathbb{R}^3$ represent the variation of $\mathbf{F}_m$ and $\boldsymbol{\tau}_m \in \mathbb{R}^3$ with respect to a local configuration change.

By inverting the Jacobian (using a damped least-squares approach), we compute $\delta\mathbf{p}_E$ and $\delta\widehat{\mathbf{m}_E}$, favoring rotation for torque control to maintain the EPM's position directly above the IPM. Further details on force/torque control, including how the dipole-dipole model was used to determine the motion of the EPM and the robot joints necessary to control the IPM, as well as the real-time 6 DoFs localization system, were presented in previous work (3).

Oloid Shape Integration

While the pure oloid provides a theoretical maximum range of 360° rotation and roll stability, incorporating essential magnetic endoscopic components such as a camera, LED, IPM with localization, tubes for insufflation, irrigation, and Camera Cleaning requires enlarging the device beyond a clinically practical size. Conversely, cylindrical designs accommodate these components but offer no controlled rolling motion. Embedding the oloid within a cylindrical form retains essential rolling capabilities while maintaining a practical device size, achieving a balanced hybrid design suitable for clinical applications.

These generator lines that develop the oloid's surface determine its interaction with surfaces, allowing for a smooth rolling motion as each line sequentially contacts the surface. The extent of these lines on a device determines its range of motion. In a single EPM system like the MFE, the endoscope is primarily attracted to the upper surface of the environment, specifically the top half of the lumen of the colon. Thus, only the upper surface of the endoscope required functionalization, incorporating two of the four quadrants of the oloid shape. To maintain pure tilt control from a neutral position, a flat chamfer was added to the top edge of the oloid shape.

The OME was manufactured using a 3D printed resin shell (Form 3+, Formlabs). The resulting OME, shown in

Figure 2C(ii), has compact dimensions of 20 mm x 20 mm x 35 mm in line with the previous MFE design.

Ultrasound Integration

The µUS probe incorporated into the OME was a commercially supplied 28 MHz, 128-element linear array (L28SXTech, VERMON S.A) that was adapted for the application. Microcoaxial cables (42 AWG - Alpha Wire) were directly soldered to the flexible Printed Circuit Board (PCB) pads corresponding to the array elements, with an additional cable for the PCB's ground connection. The microcoaxial cables from the array were terminated with LEMO connectors and connected to the Verasonics controller for US transmission and data acquisition.

Modifications were made to the OME design to accommodate the µUS probe resulting in the OME-U (Figure 2C(iii)), comprising a detachable section incorporating the sensor. This design choice was driven by sustainability considerations to facilitate the testing and reuse of various sensors, while the main endoscope can be discarded as its lumens are difficult to clean. This also ensures that the endoscope remains adaptable and versatile for different medical applications.

The array was driven using a synthetic aperture protocol (*45*) modified to use five transmitting elements (Tx) in parallel and all receive elements (Rx) for each acquisition to maintain electrical power levels within reasonable bounds, while improving the Signal to Noise Ratio (SNR) compared to the conventional US B-mode imaging protocol that uses only one Tx element per acquisition (*46*). The magnitude of the Tx signal was set to 20 V_{peak} and the frame rate of the imaging system was ~9 Hz, compatible with the speed of motion of the OME-U. The real-time generated B-scans or 2D µUS images were transmitted over ROS and post-processed using logarithmic time gain compensation (TGC) for improved contrast.

In vivo Trials for Roll and Sweep

The trials were conducted on a 39 kg pig under general anesthesia at the Large Animal Experimental Facility, University of Leeds. These trials were carried out under Project Licence PC71ADE55, approved by the University of Leeds (establishment license number XDE639D76) in compliance with the Home Office (UK) legislation, the Animal (Scientific Procedures) Act 1986, and NC3Rs guidelines. This report adheres to the ARRIVE guidelines.

After cleaning the colon through multiple rounds of enema, the OME was inserted through the rectum into the colon and advanced to about 20 cm beyond the rectum. This distance provided a long, straight region of the bowel for experimentation. The OME was followed with a standard endoscope (Olympus PCF-160AL) to render rear visualization of the OME and surrounding tissue. The ancillary elements of the OME were used for distension of the colon and irrigation when necessary.

The main objectives of these trials were to demonstrate that the OME can be successfully manipulated in the roll direction in vivo and that it can perform clinically applicable motions for contact-based sensing. Two experiments were designed to provide proof. The first consisted in a sweeping motion across the upper half of the colon surface, and the second involved a pure rolling motion within a ±50° roll. Each experiment was repeated five times. After the experiments were completed, the OME was removed by pulling it from its soft tether. Then, the standard endoscope was used to scan the colon surface to assess damage, with no evidence observed.

Contact Detection

To enable autonomous sweeping, a contact detection algorithm (see Supplementary Methods) was developed to assess the quality of contact between the µUS array and the tissue. This evaluation was crucial for the control loop that ensured continuous imaging by compensating for any loss of contact during sweeping.

For precise contact detection, µUS images underwent initial cropping to isolate a specific "zone of interest". This zone typically encompassed the region from 0% to 7% of the image depth, where differences indicative of contact versus no contact were most discernible. These differences were particularly noticeable due to an increase in high-intensity reverberations near the array's surface when the device was not in contact with the tissue, a phenomenon caused by the large difference in acoustic impedance between the array material and air.

By extracting the maximum value from each column in the µUS image, corresponding to one of the 32 µUS array elements, and applying binary thresholding, the system computed an average contact value ranging from 0 ("decoupled") to 1 ("coupled"). The algorithm represented the detected coupling quality through a color-coded bar overlaid on the µUS image (Figure S7). This bar offered immediate feedback by transitioning from green, indicating good coupling, to red, indicating poor coupling, thus visually conveying the level of contact to the operator.

Given the variation in contact quality across different testing surfaces, such as silicone phantoms and in vivo mucosal tissue, calibration was necessary to determine the exact "zone of interest" and the appropriate threshold levels for the contact value. This calibration process involved performing a sequence of five coupling-decoupling repetitions to establish these

critical parameters. Adjustments were based both on the observed differences in the µUS images and the contact value output.

Autonomous Sweeping

The autonomous sweeping algorithm consisted of three stages: initialization, contact recovery and execution of a pre-planned sweeping motion. Initialization set the correct frame of reference ($\mathbf{R}_D$) for the sweep motion, accommodating the variable orientation of the colon in vivo, which cannot be predetermined without supplementary imaging such as CT scans. Using the localization system and WLI, the operator positioned the OME-U centrally within the lumen before beginning the sweep, thereby establishing an initial reference frame relative to the global frame.

Once initialized, the algorithm checked the contact quality between the array and the tissue. If the contact was insufficient, the algorithm entered a contact recovery mode, applying magnetic torque about the tilt axis to improve proximity to the GI wall. Once adequate contact was achieved, the OME-U proceeded with the pre-planned sweeping motion, which involved a combination of horizontal translation and roll. This motion continued as long as contact remained adequate; if not, the algorithm reverted to contact recovery mode. This autonomous strategy, leveraging the oloid shape, WLI, robotic adjustments, and the µUS array feedback, enabled consistent, high-quality imaging of the colon wall. Benchtop validation of the autonomous sweeping is detailed in Figures S6, S7, and Supplementary Methods.

3D Reconstruction

Using the 2D µUS images acquired from the autonomous sweep of the porcine colon with the OME-U, a 3D visualization of the scanned colon section was created. A custom MATLAB script was developed to extract robot positional information corresponding to each image in the dataset, ensuring precise spatial alignment during reconstruction. This process entailed iterating through all the images, reading each image in turn from the specified directory, and adjusting its position based on the corresponding robot position. An interpolation was then used to fill the gaps in the 3D projection of the image stack. Detailed steps are provided in Figure S9 and Supplementary Methods.

By adjusting thresholds, specific pixel intensities were targeted to generate an isosurface, which is a 3D surface representation of points with equal values (isovalue) in a 3D intensity volume. The isovalue could be easily adjusted by the user to suit different scenarios and enhance visualization. For the results illustrated in Figure 8, using the same isovalue in both the cases, greatly emphasized the depiction of the polyp in Figure 8D.

An analysis was conducted to assess the accuracy and reliability of the reconstructed tissue volume (see Figure S10 and Supplementary Methods). Metrics such as spatial fidelity and volumetric accuracy were evaluated to quantify the performance of the reconstructed polyp. Spatial fidelity was established during the benchtop phantom trial, where all measurements were controlled. The OME-U was fixed to a motor and rotated at a constant speed while maintaining constant contact with the silicon phantom. Ensuring a constant speed allowed for a reconstruction where the voxels have the same size, validating the algorithm's ability to reconstruct volumes and assess its precision by comparing the obtained dimensions of known high-echogenicity elements included in the phantom. These experiments determined the accuracy of the spatial reconstruction across different trials.

The spatial resolution of the 3D scan reconstruction depended on the image resolution along the x and y axes, and the accuracy of localization along the z-axis, as shown in Figure 8, which was influenced by the differences between successive OME-U pose values. Volumetric accuracy was assessed by reconstructing the inner volume of the polyp after characteristic feature extraction and comparing it with the volume of the solution injected to create the polyp. Once the features were extracted from the reconstructed volume, it became possible to save them and process this information in the form of a 3D object. From this, the contents could be extracted by subtraction to determine the volume contained in the polyp, which was then compared to the actual volume.

Supplementary Materials

The PDF file includes:

Supplementary Discussion
Supplementary Figures
Supplementary Methods
Table S1
Figures S1 to S11

Other Supplementary Material for this manuscript includes the following:

Movies S1 to S6 (https://www.youtube.com/playlist?list=PLWtIpCj5v7Nez_fUVWN239PC-4kG1nhsh).

References

1. G. Pittiglio, J. H. Chandler, T. da Veiga, Z. Koszowska, M. Brockdorff, P. Lloyd, K. L. Barry, R. A. Harris, J. McLaughlan, C. Pompili, P. Valdastri, Personalized magnetic tentacles for targeted photothermal cancer

therapy in peripheral lungs. *Commun Eng* **2**, 1–13 (2023).
2. R. Dreyfus, Q. Boehler, S. Lyttle, P. Gruber, J. Lussi, C. Chautems, S. Gervasoni, J. Berberat, D. Seibold, N. Ochsenbein-Kölble, M. Reinehr, M. Weisskopf, L. Remonda, B. J. Nelson, Dexterous helical magnetic robot for improved endovascular access. *Sci. Robot.* **9**, eadh0298 (2024).
3. J. C. Norton, P. R. Slawinski, H. S. Lay, J. W. Martin, B. F. Cox, G. Cummins, M. P. Y. Desmulliez, R. E. Clutton, K. L. Obstein, S. Cochran, P. Valdastri, Intelligent magnetic manipulation for gastrointestinal ultrasound. *Science Robotics* **4**, eaav7725 (2019).
4. N. G. Kim, N. J. Greenidge, J. Davy, S. Park, J. H. Chandler, J.-H. Ryu, P. Valdastri, External Steering of Vine Robots via Magnetic Actuation. *Soft Robotics*, doi: 10.1089/soro.2023.0182 (2024).
5. M. Mattille, Q. Boehler, J. Lussi, N. Ochsenbein, U. Moehrlen, B. J. Nelson, Autonomous Magnetic Navigation in Endoscopic Image Mosaics. *Advanced Science* **n/a**, 2400980.
6. C. Spada, S. Piccirelli, C. Hassan, C. Ferrari, E. Toth, B. González-Suárez, M. Keuchel, M. McAlindon, Á. Finta, A. Rosztóczy, X. Dray, D. Salvi, M. E. Riccioni, R. Benamouzig, A. Chattree, A. Humphries, J.-C. Saurin, E. J. Despott, A. Murino, G. W. Johansson, A. Giordano, P. Baltes, R. Sidhu, M. Szalai, K. Helle, A. Nemeth, T. Nowak, R. Lin, G. Costamagna, AI-assisted capsule endoscopy reading in suspected small bowel bleeding: a multicentre prospective study. *The Lancet Digital Health* **6**, e345–e353 (2024).
7. J. J. Abbott, E. Diller, A. J. Petruska, Magnetic Methods in Robotics. *Annual Review of Control, Robotics, and Autonomous Systems* **3**, 57–90 (2020).
8. E. Diller, J. Giltinan, G. Z. Lum, Z. Ye, M. Sitti, Six-degree-of-freedom magnetic actuation for wireless microrobotics. *The International Journal of Robotics Research* **35**, 114–128 (2016).
9. C. R. Thornley, L. N. Pham, J. J. Abbott, Reconsidering Six-Degree-of-Freedom Magnetic Actuation Across Scales. *IEEE Robotics and Automation Letters* **4**, 2325–2332 (2019).
10. C. Xu, Z. Yang, G. Z. Lum, Small-Scale Magnetic Actuators with Optimal Six Degrees-of-Freedom. *Advanced Materials* **33**, 2100170 (2021).
11. J. Giltinan, M. Sitti, Simultaneous Six-Degree-of-Freedom Control of a Single-Body Magnetic Microrobot. *IEEE Robotics and Automation Letters* **4**, 508–514 (2019).
12. A. J. Petruska, Open-Loop Orientation Control Using Dynamic Magnetic Fields. *IEEE Robot. Autom. Lett.* **5**, 5472–5476 (2020).
13. H. Wang, J. Cui, K. Tian, Y. Han, Three-degrees-of-freedom orientation manipulation of small untethered robots with a single anisotropic soft magnet. *Nat Commun* **14**, 7491 (2023).
14. OctoMag: An Electromagnetic System for 5-DOF Wireless Micromanipulation | IEEE Journals & Magazine | IEEE Xplore. https://ieeexplore.ieee.org/abstract/document/5595508?casa_token=6EhIB2JQ0AIAAAAA:d8XaznisQORCq4wKFMjJyxKsqVVZ8JUlud7Ri26FoJW7nu51ffBXq0zUiXBX8Chzz_X0YIYa.
15. O. Erin, X. Chen, A. Bell, S. Raval, T. Schwehr, X. Liu, P. Addepalli, L. O. Mair, I. N. Weinberg, Y. Diaz-Mercado, A. Krieger, Strong magnetic actuation system with enhanced field articulation through stacks of individually addressed coils. *Sci Rep* **14**, 23123 (2024).
16. L. Song, Y. Dai, L. Wang, W. Zhang, Y. Ji, Y. Cao, J. Wei, F. Wang, J. Zhong, J. Yang, L. Feng, Motion Control of Capsule Robot Based on Adaptive Magnetic Levitation Using Electromagnetic Coil. *IEEE Transactions on Automation Science and Engineering* **20**, 2720–2731 (2023).
17. Y. Huo, L. Yang, T. Xu, D. Sun, Design, Control, and Clinical Applications of Magnetic Actuation Systems: Challenges and Opportunities. *Advanced Intelligent Systems* **n/a**, 2400403.
18. A. W. Mahoney, J. J. Abbott, Five-degree-of-freedom manipulation of an untethered magnetic device in fluid using a single permanent magnet with application in stomach capsule endoscopy. *The International Journal of Robotics Research* **35**, 129–147 (2016).
19. K. Obstein, C. Landewee, J. Norton, J. Martin, S. Caló, J. W. Kow, B. Scaglioni, P. Valdastri, The Magnetic Flexible Endoscope: Phase 1 First-In-Human Trial. *Gastrointestinal Endoscopy* **99**, AB581 (2024).
20. J. W. Martin, L. Barducci, B. Scaglioni, J. C. Norton, C. Winters, V. Subramanian, A. Arezzo, K. L. Obstein, P. Valdastri, Robotic Autonomy for Magnetic Endoscope Biopsy. *IEEE Transactions on Medical Robotics and Bionics* **4**, 599–607 (2022).
21. K. Simon, Colorectal cancer development and advances in screening. *Clin Interv Aging* **11**, 967–976 (2016).
22. L. J. Sliker, G. Ciuti, Flexible and capsule endoscopy for screening, diagnosis and treatment. *Expert Rev Med Devices* **11**, 649–666 (2014).
23. T. M. H. Gall, S. R. Markar, D. Jackson, A. Haji, O. Faiz, Mini-probe ultrasonography for the staging of colon cancer: a systematic review and meta-analysis. *Colorectal Dis* **16**, O1-8 (2014).
24. H. Seifert, P. Fusaroli, P. G. Arcidiacono, B. Braden, F. Herth, M. Hocke, A. Larghi, B. Napoleon, M. Rimbas, B. S. Ungureanu, A. Săftoiu, A. V. Sahai, C. F. Dietrich, Controversies in EUS: Do we need miniprobes? *Endosc Ultrasound* **10**, 246–269 (2021).
25. ExactVu™ Micro-Ultrasound System - Exact Imaging. https://www.exactimaging.com/exactvu-micro-ultrasound-system.
26. R. Vassallo, T. A. Aleef, Q. Zeng, B. Wodlinger, P. C. Black, S. E. Salcudean, Robotically controlled three-dimensional micro-ultrasound for prostate biopsy guidance. *Int J CARS* **18**, 1093–1099 (2023).
27. H. S. Lay, B. F. Cox, V. Seetohul, C. E. M. Démoré, S. Cochran, Design and Simulation of a Ring-Shaped Linear Array for Microultrasound Capsule Endoscopy. *IEEE Transactions on Ultrasonics, Ferroelectrics, and Frequency Control* **65**, 589–599 (2018).
28. X. Wang, V. Seetohul, R. Chen, Z. Zhang, M. Qian, Z. Shi, G. Yang, P. Mu, C. Wang, Z. Huang, Q. Zhou, H. Zheng, S. Cochran, W. Qiu, Development of a Mechanical Scanning Device With High-Frequency Ultrasound Transducer for Ultrasonic Capsule Endoscopy. *IEEE Trans Med Imaging* **36**, 1922–1929 (2017).

29. Y. I. Sobolev, R. Dong, T. Tlusty, J.-P. Eckmann, S. Granick, B. A. Grzybowski, Solid-body trajectoids shaped to roll along desired pathways. *Nature* **620**, 310–315 (2023).
30. S. Jeon, A sphericon-shaped magnetic millirobot rolling on a surface actuated by an external wobbling magnetic field. *AIP Advances* **7**, 056708 (2017).
31. A. Petruska, J. Abbott, Optimal Permanent-Magnet Geometries for Dipole Field Approximation. *Magnetics, IEEE Transactions on* **49**, 811–819 (2013).
32. M. Miyasaka, P. Berkelman, Magnetic levitation with unlimited omnidirectional rotation range. *Mechatronics* **24** (2014).
33. H. Dirnbock, H. Stachel, The Development of the Oloid. *Journal for Geometry and Graphics* **1** (1997).
34. M. J. Gora, M. J. Suter, G. J. Tearney, X. Li, Endoscopic optical coherence tomography: technologies and clinical applications [Invited]. *Biomed Opt Express* **8**, 2405–2444 (2017).
35. S. W. Yoo, G. Oh, A. M. Safi, S. Hwang, Y.-S. Seo, K.-H. Lee, Y. L. Kim, E. Chung, Endoscopic non-ablative fractional laser therapy in an orthotopic colon tumour model. *Sci Rep* **8**, 1673 (2018).
36. A. Bouakaz, J. Michel Escoffre, From concept to early clinical trials: 30 years of microbubble-based ultrasound-mediated drug delivery research. *Advanced Drug Delivery Reviews* **206**, 115199 (2024).
37. S. Hernot, A. L. Klibanov, Microbubbles in ultrasound-triggered drug and gene delivery. *Advanced Drug Delivery Reviews* **60**, 1153–1166 (2008).
38. J. W. Martin, B. Scaglioni, J. C. Norton, V. Subramanian, A. Arezzo, K. L. Obstein, P. Valdastri, Enabling the future of colonoscopy with intelligent and autonomous magnetic manipulation. *Nat Mach Intell* **2**, 595–606 (2020).
39. P. Valdastri, M. Simi, R. J. Webster, Advanced Technologies for Gastrointestinal Endoscopy. *Annual Review of Biomedical Engineering* **14**, 397–429 (2012).
40. A. Wilson, B. P. Saunders, Position change during colonoscopy: the oldest and best trick in the book. *Gastrointestinal Endoscopy* **82**, 495–496 (2015).
41. K. L. Andersson, J. B. Ha, D. R. Abraczinskas, E. J. Campbell, J. M. Richter, Gender Differences in Colonoscopy: Implications for Clinical Practice and Female Gastroenterologists. *Dig Dis Sci* **67**, 810–816 (2022).
42. I. Hiroshi, The Development of the Two-Circle-Roller in a Numerical Way (2011). http://ilabo.bufsiz.jp/Development/2c-english.pdf.
43. A. S. Kuleshov, M. Hubbard, D. L. Peterson, G. Gede, "On the motion of the Oloid toy" in *XXXIX International Summer School–Conference APM 2011* (2011), p. 8.
44. A. Z. Taddese, P. R. Slawinski, M. Pirotta, E. De Momi, K. L. Obstein, P. Valdastri, Enhanced real-time pose estimation for closed-loop robotic manipulation of magnetically actuated capsule endoscopes. *The International Journal of Robotics Research* **37**, 890–911 (2018).
45. T. L. Szabo, "10 - Imaging Systems And Applications" in *Diagnostic Ultrasound Imaging*, T. L. Szabo, Ed. (Academic Press, Burlington, 2004; https://www.sciencedirect.com/science/article/pii/B9780126801453500116)*Biomedical Engineering*, pp. 297–336.
46. A. C. Moldovan, B. Abaravičius, S. Mitra, S. Cochran, "Power Consumption Considerations for Ultrasound Capsule Endoscopy" in *2023 IEEE International Ultrasonics Symposium (IUS)* (IEEE, Montreal, QC, Canada, 2023; https://ieeexplore.ieee.org/document/10306773/), pp. 1–4.

Acknowledgments:
We thank Dr. Joseph Norton, Dr. Khawar Abbas, Samwise Wilson and Joshua Davy for their support. Figure 1 was created using CAD files obtained from GrabCAD and Sketchfab (https://skfb.ly/6Vpyr), in accordance with their respective Creative Commons licenses.

Funding:
This work was supported in part by the Engineering and Physical Sciences Research Council (EPSRC) under Grants EP/Y037235/1 and EP/V047914/1, the European Research Council (ERC) through the European Union's Horizon 2020 Research and Innovation Programme under Grant 818045, the European Commission (EC) through the European Union's Horizon 2020 Research and Innovation Programme under Grant 952118, and by the National Institute for Health and Care Research (NIHR) Leeds Biomedical Research Centre (BRC) (NIHR203331). Any opinions, findings and conclusions, or recommendations expressed in this article are those of the authors and do not necessarily reflect the views of the EPSRC, the ERC, the EC or the NIHR.

Author contributions:
Conceptualization: NJG, PV
Methodology: NJG, BC, JWM, NM, DV
Investigation: NJG, BC, ACM, BA, JWM
Visualization: NJG, BC
Funding acquisition: SM, SC, PV
Project administration: NJG, SC, PV
Supervision: BS, SM, SC, PV
Writing – original draft: NJG, BC, ACM
Writing – review & editing: NJG, BC, ACM, BA, JW, BS, SC, PV

Data and materials availability:
All data needed to evaluate the conclusions in this paper are present in the paper or the Supplementary Materials including the deposit in the Dryad database (https://doi.org/10.5061/dryad.t1g1jwtbx).

Supplementary Materials for

Harnessing the oloid shape in magnetically driven robots to enable high-resolution ultrasound imaging

Nikita J. Greenidge *et al.*

Corresponding author: Nikita J. Greenidge, elnjg@leeds.ac.uk

The PDF file includes:

Other Supplementary Materials for this manuscript include the following:

Movies S1 to S6
(https://www.youtube.com/playlist?list=PLWtIpCj5v7Nez_fUVWN239PC-4kG1nhsh)

Addressing the DoF Limitation in Magnetic Manipulation

In an attempt to minimize the potential energy between an external magnetic field $\mathbf{B}_{\boldsymbol{E}} \in \mathbb{R}^3(\mathrm{T})$ generated by the controlling source (external dipole) and a magnetic object (internal dipole) with magnetic moment, $\mathbf{m}_{\mathrm{I}} \in \mathbb{R}^3(\mathrm{A} \cdot \mathrm{m}^2)$, an alignment torque $\boldsymbol{\tau}_{\mathrm{m}}$ is induced on the magnetic object and is given by:

$$\boldsymbol{\tau}_{\mathrm{m}} = \mathbf{m}_{\mathrm{I}} \times \mathbf{B}_{\boldsymbol{E}} = S(\mathbf{m}_{\mathrm{I}})\mathbf{B}_{\boldsymbol{E}} \tag{1}$$

where $S(\cdot)\colon \mathbb{R}^3 \mapsto \mathbb{R}^{3\times 3}$ is the skew-symmetric matrix operator. The gradient-induced force exerted on the magnetic object is denoted by $\mathbf{F}_{\mathrm{m}}$:

$$\mathbf{F}_{\mathrm{m}} = \nabla(\mathbf{B}_{\boldsymbol{E}} \cdot \mathbf{m}_{\mathrm{I}}) \tag{2}$$

In the magnetic object's local coordinate frame with orthonormal vectors $\mathbf{X}_{\boldsymbol{I}}, \mathbf{Y}_{\mathrm{I}}$, and $\mathbf{Z}_{\mathrm{I}} \in \mathbb{R}^3$, Euler angles, ϕ, θ and ψ denote the rotation around these vectors (Figure 3). Conventionally, $\mathbf{X}_{\boldsymbol{I}} \parallel \mathbf{m}_{\mathrm{I}}$ (as shown in Figure 1 and 3), but when $\mathbf{m}_{\mathrm{I}} \parallel \mathbf{B}_{\boldsymbol{E}}$ then according to Equation 1, $\boldsymbol{\tau}_{\mathrm{m}} = \mathbf{0}$. Consequently, it is not possible to generate magnetic alignment torque around the magnetization axis to control the roll angle (ϕ).

Paper	Magnetic Workspace	Environment	Required magnetically controllable inputs	Applied field	Maximum Power	Roll
Wang et. al (13)	100 x 100 x 100 mm^3	Water	8	N/A	1.4 kW	Yes
Xu et al (10)	N/A	Non-Newtonian fluid (paraffin oil, glycerol)	8	20 mT	6 kW	Yes
Diller et al (8)	20 × 20 × 20 mm^3	Silicone oil	8	8.3 mT	N/A	Yes
Giltinan et al (11)	1000 mm^3	Silicone oil	8	22 mT	6 kW	Yes
Taddese et al (44)	300 x 300 x 150 mm^3 *	In vivo - colon	5	25 mT	1-1.5 kW	No

This work	300 x 300 x 150 mm^3 *	In vivo - colon	5	25 mT	1-1.5 kW	Yes

Table S1: Roll Approaches Comparison. All values were estimated based on the details provided in the respective papers. N/A – information not provided. *This workspace is based on the static range of the EPM which can be moved within a larger workspace (1000 x 800 x 800 mm^3) due to the mobility provided by the robot arm.

As discussed in the manuscript, other methods have primarily been demonstrated in fluid environments where force and torque requirements are low. These systems typically rely on electromagnetic coil systems, requiring eight magnetically controllable inputs, leading to high power consumption and limited workspaces compared to single EPM systems. Table S1 highlights how the introduction of roll in the single EPM system represents a significant improvement over previous approaches. In electromagnetic coil systems, the workspace and applied field are proportional to power consumption.

Roll Generation in the Oloid

By concatenating orthonormal basis vectors of $\mathbb{R}^3$ we can formulate a rotation matrix, $\mathbf{R}_{\mathrm{O}}^{\mathrm{F}}$ which can be expressed as:

$$\mathbf{R}_{\mathrm{O}}^{\mathrm{F}} = [\hat{\mathbf{x}}_O \quad \hat{\mathbf{y}}_O \quad \hat{\mathbf{z}}_{\mathrm{O}}].$$

If:

The oloid is magnetized about the **x**-axis $\hat{\mathbf{x}}_O \parallel \mathbf{m}$, and

It rotates about the line $\mathbf{p}_2 - \mathbf{p}_1$, then

Its orientation can be controlled so long as $\hat{\mathbf{x}}_{\mathrm{O}} \nparallel \mathbf{p}_2 - \mathbf{p}_1$.

In other words, rotation can be induced so long as $\hat{\mathbf{x}}_{\mathrm{O}}$ is not perpendicular to the surface normal $\hat{\mathbf{z}}_{\mathrm{F}}$:

$$\hat{\mathbf{x}}_{\mathrm{O}} \perp\!\!\!/ \hat{\mathbf{z}}_{\mathrm{F}} \Longrightarrow \hat{\mathbf{x}}_{\mathrm{O}}^{\mathrm{T}} \hat{\mathbf{z}}_{\mathrm{F}} \neq \mathbf{0}$$

Where $\hat{\mathbf{z}}_{\mathrm{F}}$ is equivalent to the z-axis of {F}.

From inspection of $\mathbf{R}_{\mathrm{O}}^{\mathrm{F}}$ it must hold that:

$$-\frac{\sin(u)}{\sqrt{2(1+\cos(u))}} \neq 0 \forall u \in \left(-\frac{2\pi}{3}, 0\right) \cup \left(0, \frac{2\pi}{3}\right)$$

This is true only if:

$$\mathrm{u} = 0, \text{ or } u = \pi$$

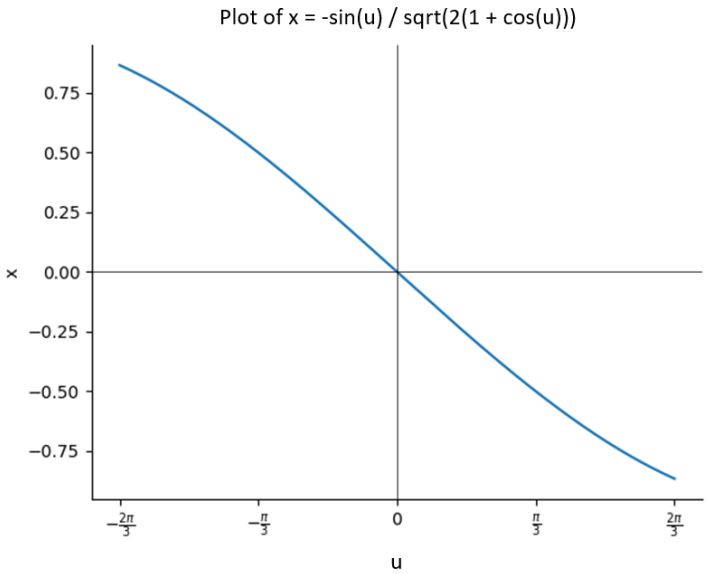

Figure S1: **Function plot over the range u.**

In a cylinder, this is true throughout the entire surface.

3 DoF Orientation Comparison between OME and MFE

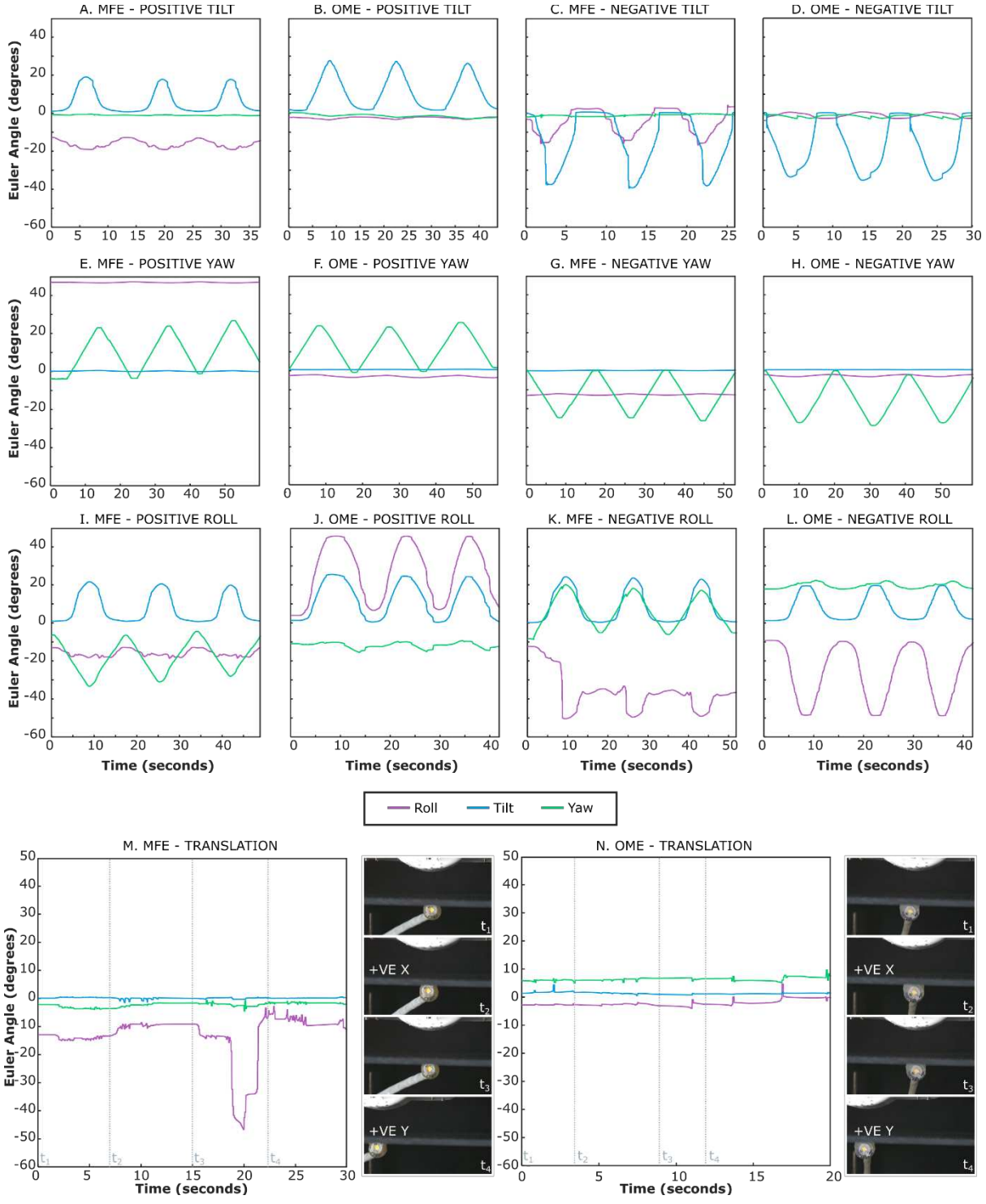

Figure S2: **3 DoF Orientation Comparison between OME and MFE.** The figure illustrates the coupling between roll, tilt and yaw, positive and negative, for both the MFE and OME. It also depicts the variation in orientation during x and y translation for both devices. See Data S2 for the corresponding multimedia.

The magnitudes of the points in the radar plot shown in Figure 4 of the manuscript were determined by calculating the average change in each DoF across the three repetitions presented for each movement in Figure S2. As evidenced by the raw data in Figure S2, the starting point for roll is consistently near zero in all the OME's movements. In contrast, the MFE exhibits arbitrary baseline values for roll initiation. Additionally, there is increased variability during movements not intended to induce roll, such as tilt and translation. Lastly, when subjected to the same input intended to trigger roll in the OME, the MFE's roll response was ineffective, especially for positive roll.

Generating Rolling Motion with the Oloid in Open-Loop

Using MFE System

Extended representation of Figure 5 in the manuscript.

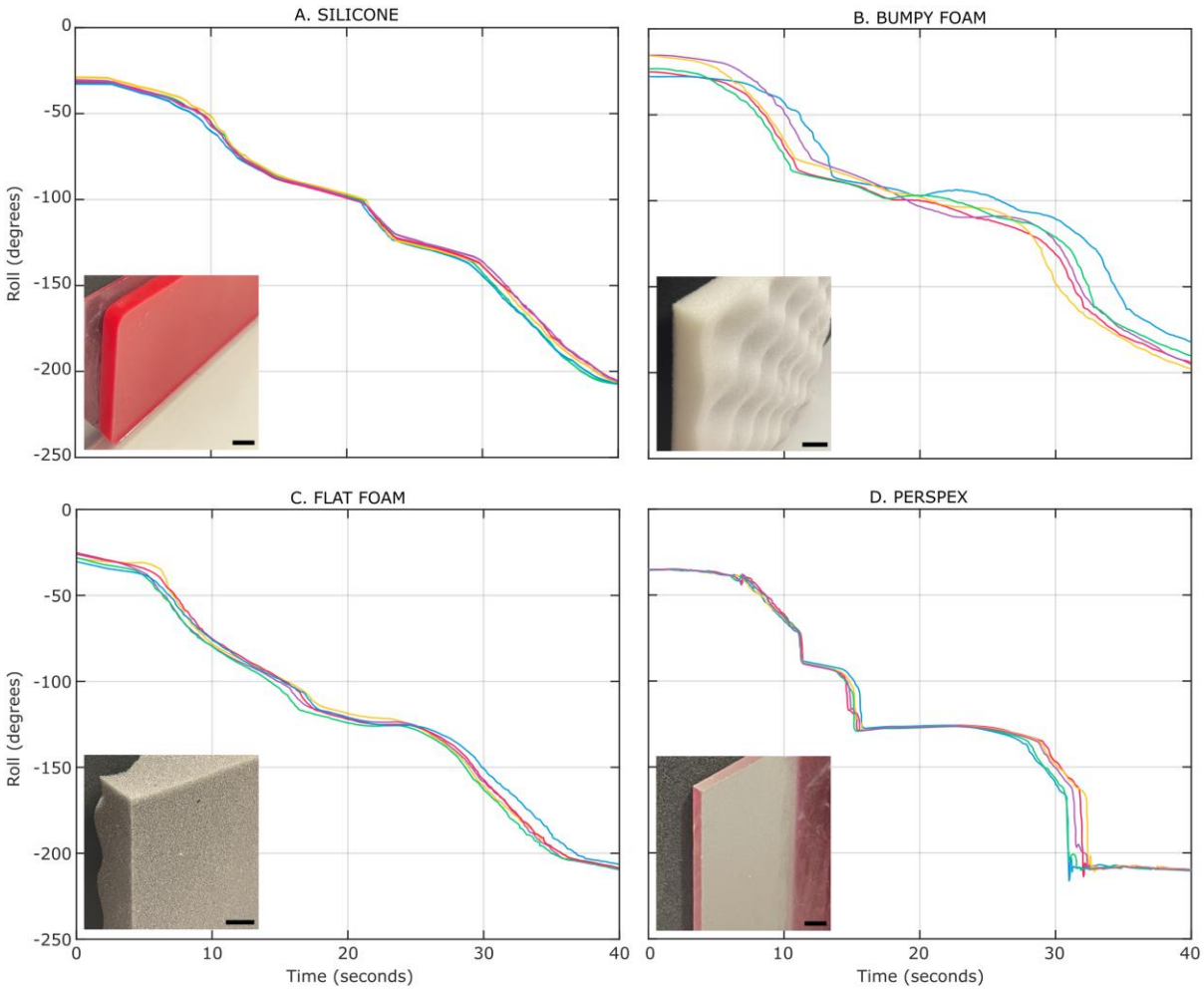

Figure S3: **Oloid Rolling on Various Surfaces.** Rolling performance of the oloid on (A) silicone, (B) bumpy foam, (C) flat foam, and (D) Perspex. Five repetitions shown for each. See Data S5 for the corresponding multimedia. Scale bars, 10 mm.

Using Electromagnetic Coil System

The oloid control model is generic and not exclusively designed for use with a robotic arm and an external permanent magnet. To support this claim, we demonstrate that, by applying a similar model to the one described in the paper, the oloid shape can perform a rolling motion on a flat surface, using electromagnetic coils. For this demonstration, a MiniMag system (MagnebotiX, Switzerland) shown in Figure S4 (A) was employed.

In order to fit this setup and to demonstrate scalability, the Oloid Magnetic Device (OMD) was scaled down to a defining oloid radius of 5 mm called the Mini-OMD. Snapshots of the rolling motion are illustrated in Figure S4 (B). This result demonstrates scalability, a tetherless configuration and that roll can be achieved with the oloid regardless of contact with the upper or lower surfaces.

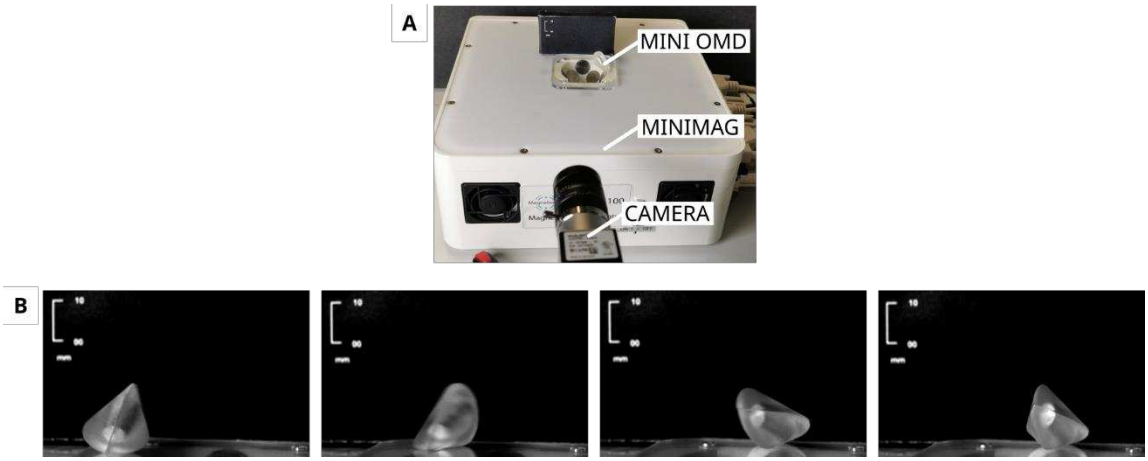

Figure S4: **Oloid Rolling in MiniMag.** (A) Experimental Setup and (B) Snapshots of a 5 mm Mini OMD rolling on a flat surface. See Data S1 for the corresponding multimedia.

Closed-Loop Control of the Oloid-shaped Magnetic Device (OMD)

Extended representation of Figure 6 in the manuscript.

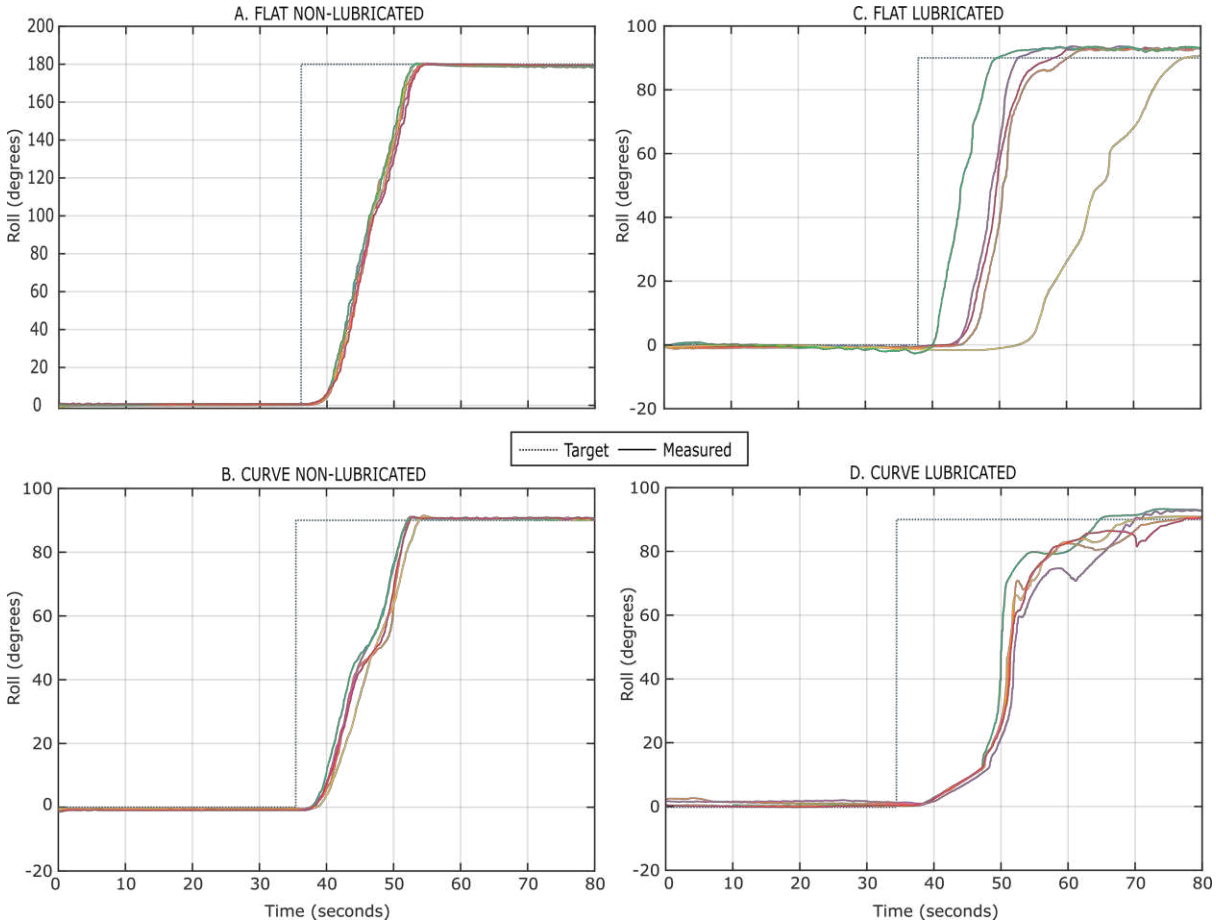

Figure S5: **Closed-loop control of the Oloid-shaped Magnetic Device (OMD)**, step input on a: (**A**) flat non-lubricated surface (**B**) curved non-lubricated surface (**C**) flat lubricated surface (**D**) curved lubricated surface. Five repetitions shown for each.

Small oscillations are observed especially on the lubricated surfaces from a combination of localization errors and inherent dynamics of the KUKA robot's control system. In scenarios involving faster environments, such as the lubricated surfaces, these oscillations become more pronounced. To reduce oscillations, KUKA's Fast Robot Interface (FRI) could be implemented in place of the current smart servo control. The FRI offers higher update rates and more precise control, which can significantly minimize oscillatory behavior by enabling faster and more accurate responses to control inputs.

Benchtop Autonomous Ultrasound Sweeping Setup

The capsule was evaluated using the platform described in Figure S6, which includes the OME-U, the KUKA LBR robotic arm, and the micro-ultrasound (μUS) system. A silicone phantom was used for benchtop trials and the initial characterization of the robotic system.

Two display monitors were employed: one for the robot control user interface and the other for ultrasound visualization.

The capsule's dexterity was recorded using a Basler Ace camera (acA2040-120uc, Basler AG, Ahrensburg, Germany), as depicted in the red square in Figure S6.

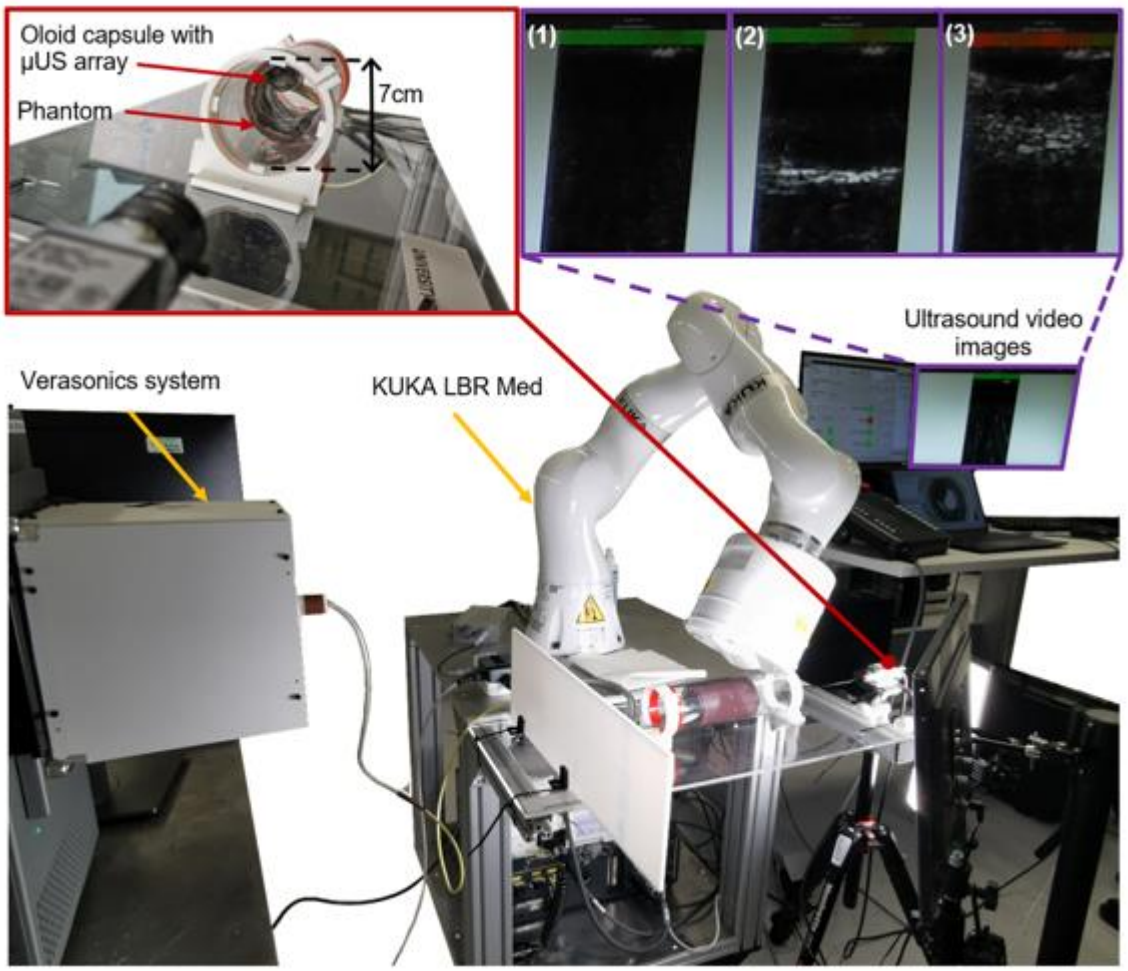

Figure S6: Detailed illustration of the experimental setup. Overview of the various components utilized during the benchtop experimentation with (red square) validation point of view for contact detection and roll/sweep performance and (purple square) snapshot depicting feedback on contact quality (1-2: good, 3: none) and visualization of the copper strip (2).

The 8 mm thick silicone phantom (Ecoflex 00-30, Smooth-on, PA, USA), utilized to validate different algorithms, was enclosed within a 7 cm inner diameter acrylic tube. Copper strips were integrated into the phantom to create components with high echogenicity, facilitating clear identification with the ultrasound probe. The white area in the second image (enclosed by the purple frame) becomes apparent when the array is oriented towards the copper strip, confirming both the proper functioning of the OME-U and the probe's ability to capture images simultaneously. The green and red bars at the top of the snapshot, enclosed by the purple frames, highlight the quality of contact between the OME and the silicone phantom.

Contact Detection Algorithm

Contact detection was performed using real-time images provided by the ultrasound probe. A series of tests was conducted on phantoms to demonstrate the effective integration of the µUS array and Verasonics acquisition of ultrasound images. The setup and phantom were used as previously described.

Figure S7 illustrates five different snapshots of the post-processed outputs using the proposed algorithm. The ultrasound images were cropped to a sector outlined in the frame where differences were most significant, approximately 7% - 30% of the image width. The maximum value for each column was then condensed to obtain the mean, resulting in values between 0 (decoupled) and 1 (coupled). The algorithm's detected coupling quality is visualized by the colored bar at the top, transitioning from green (good coupling) to red (poor coupling).

This coupling value was integrated into a control loop to enable sweeping while correcting for any loss of contact to maintain continuous imaging. This control strategy was experimentally validated by arbitrarily positioning the capsule within the tube without contact with the phantom. Using the localization system, movements of the robotic arm enabled repositioning of the capsule in contact with the tissue and initiation of the sweeping motion. Observation of the two copper strips (Figure S7.3 and S7.5) present in the silicone as the probe swept in continuous motion further validated the operation of the closed-loop control strategy for automatic imaging tasks.

During the animal trials, contact threshold parameters were calibrated by performing 10 manual repetitions:

- 5 contact recoveries with a tilt manoeuvre
- 5 contact recoveries from an upside-down configuration

These parameters were saved in the ROSbag* and implemented in the control loop. A series of 5 repetitions of autonomous sweeping were then performed, starting from no contact with the mucosa, to validate proper functioning.

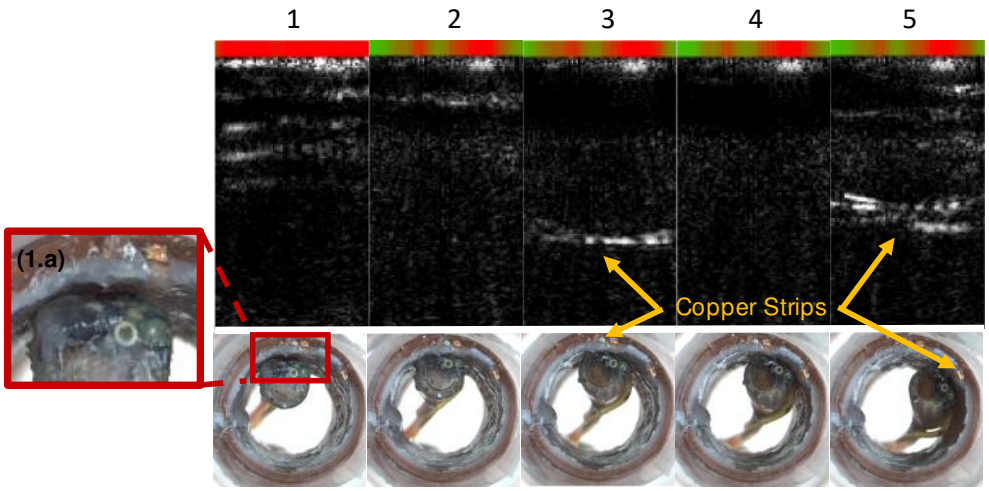

Figure S7: Illustration of the contact detection algorithm and benchtop autonomous sweeping. The snapshots illustrate sweeping from a non-contact situation highlighted in the magnified image (1.a) and by the red bar at the top of the US image to successful autonomous sweeping while keeping contact and identification of the copper strip in the phantom. See Data S3 for the corresponding data.

*A ROSbag is a file format in the Robot Operating System (ROS) used for storing ROS message data. It is essentially a log file that can record and subsequently replay ROS message streams. It enables postprocessing and analysis of the robotic systems and sensors data.

In Vivo Experimental Setup

The animal experiments were conducted in accordance with the Animal (Scientific Procedures) Act 1986, as well as the guidelines provided by NC3Rs and ARRIVE.

During the animal experimentation, the setup employed was quite similar to that described for the benchtop experiments. All procedures were recorded from both the perspective of the OME-U and an external viewpoint, utilising a standard Olympus endoscope (shown in Figure S8).

Dexterity validation experiments were initially conducted, followed by the recording of healthy tissue and probe validation and, subsequently, the creation of false polyps and scanning of them.

Real-time evaluation of all experiments was performed, and recordings were made using ROSbags (Data S4).

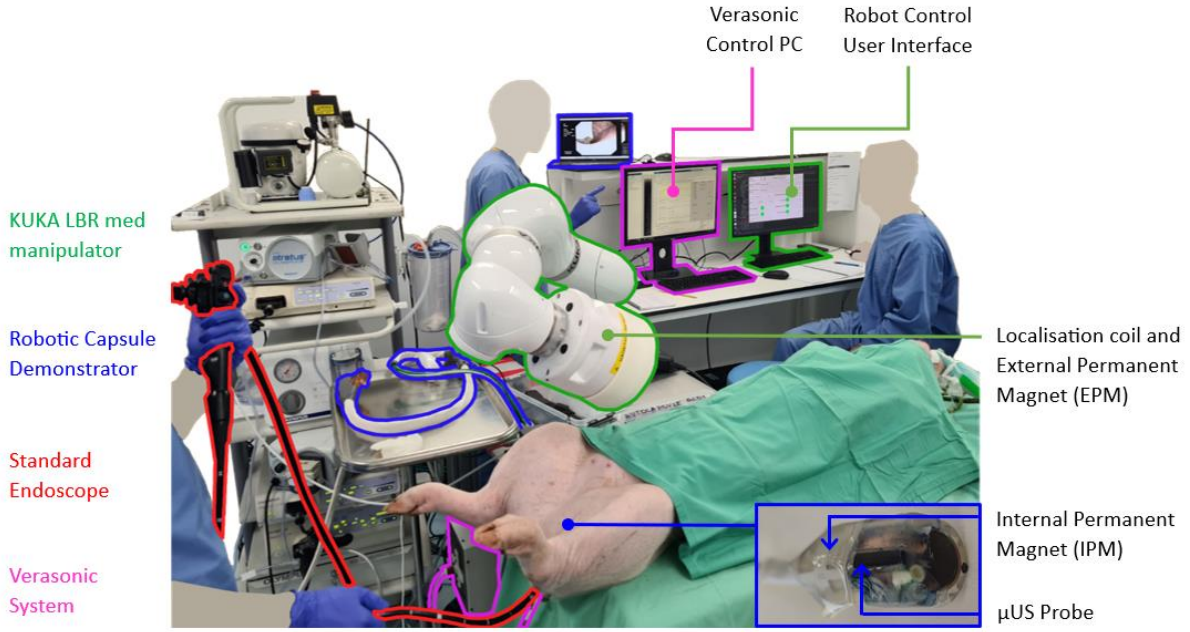

Figure S8: Detailed illustration of the in vivo setup highlighting the different devices used during the animal trial and color identification of the related parts.

Three-dimensional Subsurface Reconstruction Algorithm

This script outlines the steps involved in reconstructing a 3D volume from a series of 2D images, including reading images, adjusting positions, and visualizing the volume and its surface as shown in Figure S9.

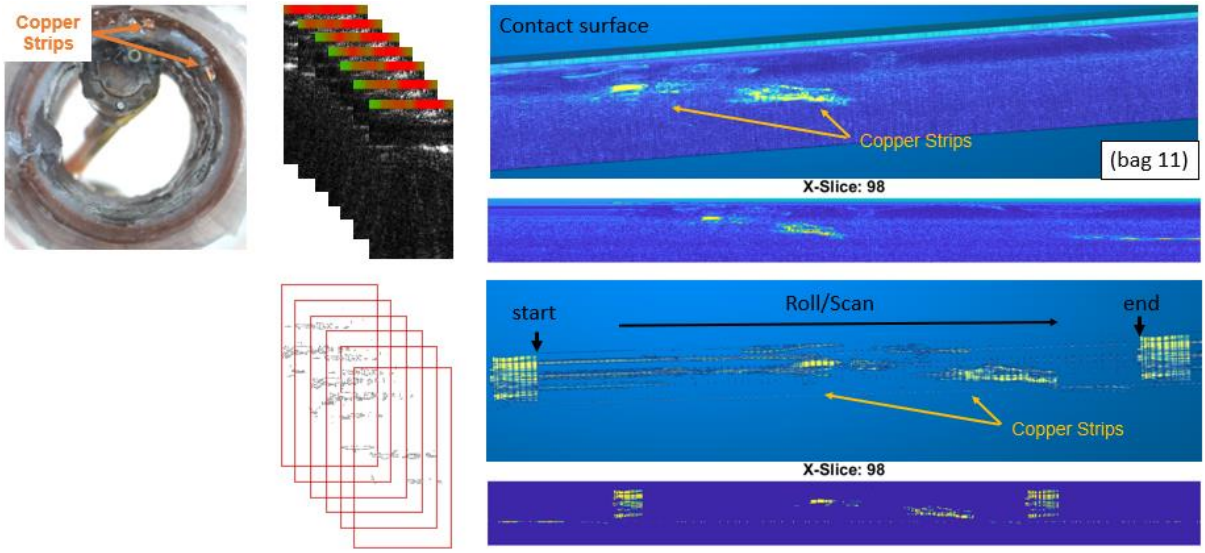

Figure S9: Detailed image reconstruction using the algorithm. Snapshot of the experimental setup on the left. Stack of images before and after extraction of the desired information in the center. Volume visualization after voxel creation before and after extraction of the desired information on the right.

1. Initialization:

- An empty matrix named 'volume' is created to store the reconstructed volume.
- Another matrix 'robotPositions' is initialized to store the positions of the robot corresponding to each image.

2. Loading ROSbag File:

- The ROSbag file named 'XXX_XXX.bag' is loaded into the workspace.

3. Reading US Images:

- All image topics present in the ROSbag file are obtained using the 'select' function, filtering by message type 'sensor_msgs/Image'.
- The images are stored in a dedicated folder.

4. Reading Robot Positions:

- There is a call of the topic 'mfe/pose' to retrieve the robot positions from the ROS bag file.
- The positions are stored in the 'robotPositions' matrix.

5. Image Processing Loop:

- The script iterates through each image.

- The file path for the image is constructed.
- The image is read.
- If the image is not grayscale, it is converted to grayscale. Additionally, the top 23 rows of the image are set to black (logical mask to false). [23 rows of contact detection]
- The position of the image is adjusted based on the robot's position.
- The adjusted image is stored in the 'volume' matrix.

6. Volume Visualization:

- The reconstructed volume is visualised.
- Various settings for visualization such as size, view angle, etc., are adjusted.

7. Surface Visualization:

- An isosurface is generated based on the volume data. The isovalue is set as a fraction of the maximum value in the volume.
- The surface is visualized using 'trimesh' function.

Benchtop 3D Reconstruction Validation

The reconstruction algorithm's spatial fidelity and accuracy were validated through two distinct approaches: utilising the robotic arm, mirroring conditions observed during animal trials, and within a controlled environment employing the setup depicted in Figure S10. For the controlled experiment, the capsule was connected to a servomotor (MX-28, ROBOTIS DYNAMIXEL) to simulate seamless motion and continuous contact.

To ensure a comparable scenario, the silicon phantom with a copper strip was employed for both experiments.

Across both setups, the positional consistency along the x and y axes remained constant, while the precision of the ultrasound (US) images remained unaffected by the robotic setup. Conversely, the accuracy along the z-axis was found to be directly influenced by the robotic platform and the coupling algorithm.

In quantifiable terms, the error of the strip width estimation using the Figure S10 setup was measured at 2%, contrasting with an 8% error when integrated into the robotic platform.

This discrepancy must be contextualised with the robot's localization capabilities, which dictate the reconstructed voxel sizes. Indeed, the 8% error falls within the expected uncertainty range of the localization system.

It should be noted that this error remained within the same order of magnitude during the in-vivo tests assessing its reliability.

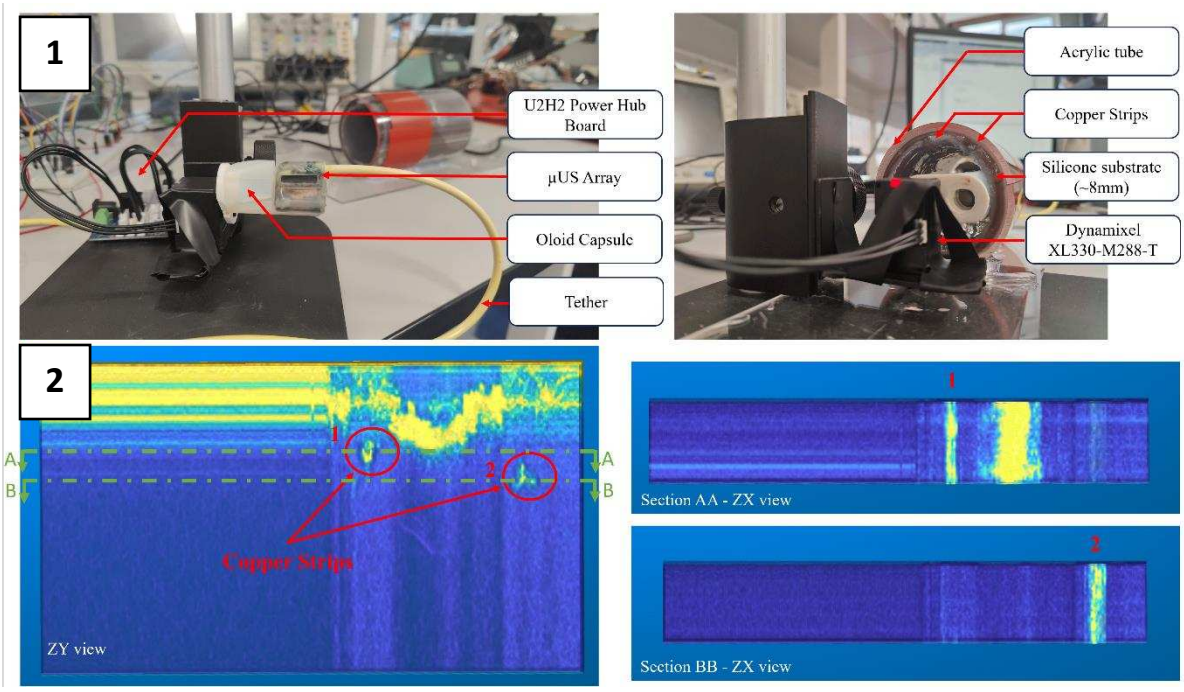

Figure S10: Calibration and evaluation setup for the reconstruction algorithm. (1) Experimental setup using a servomotor and constant speed for accuracy evaluation and threshold calibration. (2) Different views of the reconstructed volume, highlighting the reconstruction accuracy of copper strips. See Data S3 for the corresponding data.

ROS Interface

Robot Operating System (ROS) was utilized to manage all aspects of our robotic endoscope's functionality. The KUKA LBR Med R820 robot is managed in joint space through the `iiwa_stack` software package (version 1.3.0) (https://github.com/IFL-CAMP/iiwa_stack/wiki), which seamlessly integrates with ROS Melodic (Ubuntu 18.04).

MATLAB was utilized for ultrasound data processing, and the processed data were transmitted via the Olympus Decklink Mini Monitor 4K frame-grabber which interfaces with ROS for real-time processing.

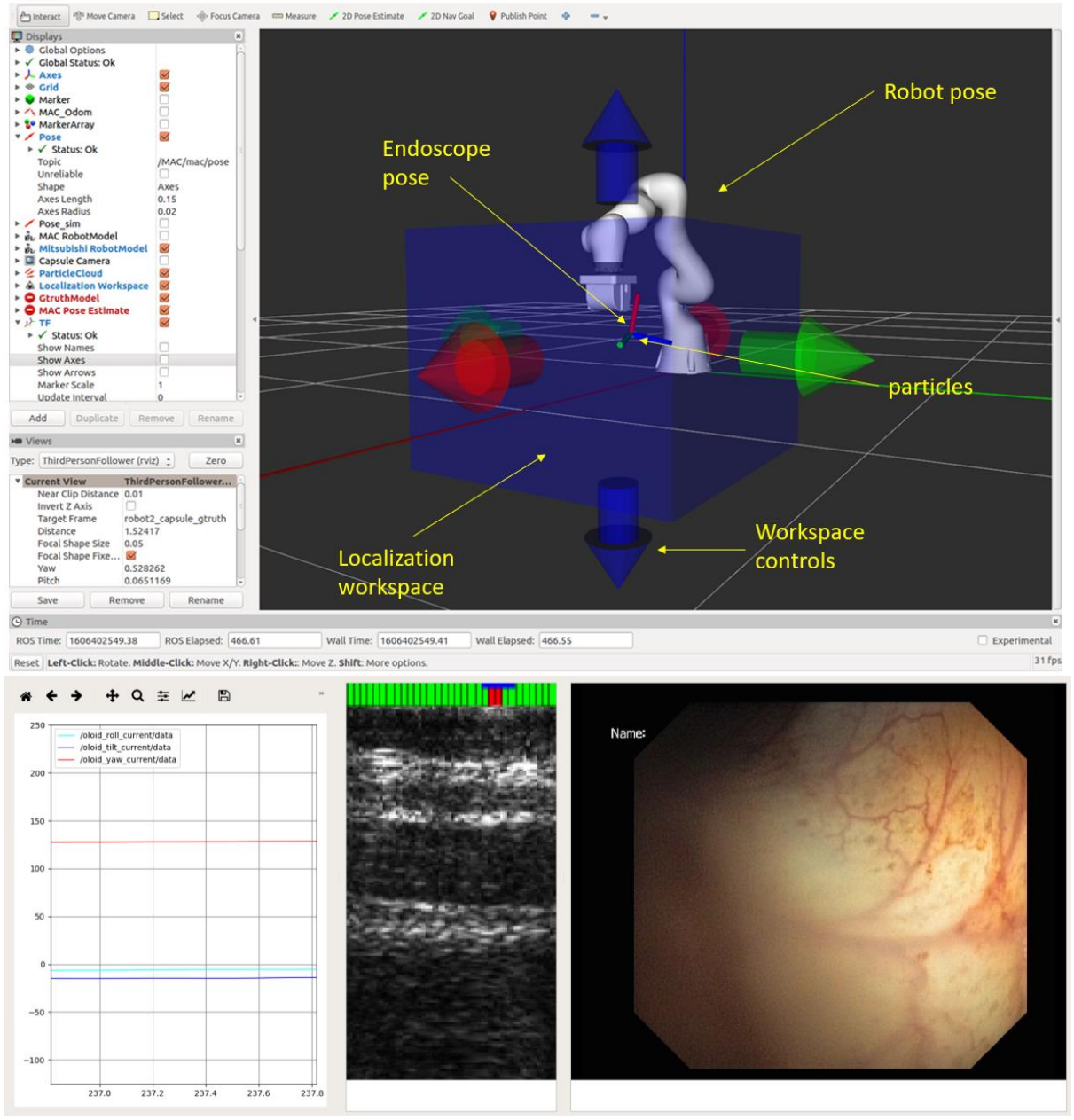

Figure S11: ROS Interface

Localization Calibration

The localization system in the endoscope is calibrated using a calibration cube precisely tailored to the endoscope's overall shape. The cube, machined from a solid block of Delrin, ensures sub-degree accuracy by providing dedicated features that secure the endoscope in a reference orientation relative to gravity. This process computes the orientation of the IMU with respect to the endoscope reference frame and the relative orientation of each sensor with respect to the IMU.

The calibration only involves orientations, and so, the position of the endoscope during calibration is not critical. The main variable affecting accuracy is the orientation of the surface upon which the cube rests during data acquisition, which should be flat with respect to gravity. The calibration process is robust, with errors up to 5% of the sensors' range having negligible effects on localization.

To address potential drift over repeated uses, the system incorporates a secondary 'on-the-fly' gyro bias removal calibration. This feature ensures consistent calibration over more than 10 procedures (typically no more than 30 minutes), with any constant bias easily detected by placing the endoscope in a known pose and verifying static accuracy. These measures ensure the robustness and reliability of the localization system, even under conditions that may introduce minor disturbances.

Other Supplementary Material

Movies:

- **Movie S1:** Concept Overview of the Oloid-Shaped Magnetic Medical Device.
- **Movie S2:** Oloid Magnetic Endoscope (OME) versus Magnetic Flexible Endoscope (MFE) Degrees of Freedom (DoFs)
- **Movie S3:** Open-Loop Control of the Oloid-Shaped Magnetic Device (OMD).
- **Movie S4:** Closed-Loop Control of the Oloid-Shaped Magnetic Device (OMD).
- **Movie S5:** *In Vivo* Rolling and Sweeping Motion of the Oloid Magnetic Endoscope (OME).
- **Movie S6:** *In Vivo* Autonomous Sweeping of the Oloid Magnetic Endoscope with Integrated Micro-Ultrasound (OME-U) and 3D Virtual Biopsy Reconstruction.

https://www.youtube.com/playlist?list=PLWtIpCj5v7Nez_fUVWN239PC-4kG1nhsh

Data:

- **Data S1: MiniMag-miniOMD.mp4:** Video showing mini-OMD oloid rolling in the MiniMag electromagnetic coil system.
- **Data S2: DOF_comparison.zip:** This folder contains video footage with live Euler angle graphs comparing the degrees of freedom (DOF) of the system under different conditions.
- **Data S3: 3D_Reconstruction.zip:** This folder contains data related to the 3D reconstruction experiments.
- **Data S4: In_vivo_-_roll_sweep.zip:** This folder contains in vivo roll sweep experiments, including .bag files, endoscopic videos and synced demonstration videos.
- **Data S5: Open_loop_roll.zip:** This folder contains videos from the open-loop roll experiments on different surfaces.
- **Data S6: Oloid_development.m:** MATLAB script to apply a transformation to a single point using Theorem 4 to handle the full transformation for the oloid geometry.
- **Data S7: Parametric_Oloid_Surface.m:** MATLAB Script to plot the oloid shape based on parametric equations.
- **Data S8: Theorem4_sym.m:** MATLAB Script with function for Theorem 4 from the paper by Dirnbock and Stachel (1997), "The Development of the Oloid" to generate the transformation matrices for the oloid's motion.

Dryad Database: https://doi.org/10.5061/dryad.t1g1jwtbx